

Black Hole Quasi-Periodic Oscillations in the Presence of Gauss–Bonnet Trace Anomaly

Rupam Jyoti Borah^{*} and Umananda Dev Goswami[†]

Department of Physics, Dibrugarh University, Dibrugarh 786004, Assam, India

We investigate the effects of the Gauss–Bonnet (GB) gravitational trace anomaly on the circular motion of test particles around black holes (BHs) and its implications for quasi-periodic oscillations (QPOs) in various theoretical models. Beginning with the equations of motion, we study the effects on effective potential, angular momentum, specific energy, and the innermost stable circular orbit (ISCO) induced by the anomaly parameter α . The fundamental frequencies are calculated. Moreover, we examine several QPO models, including PR, RP, WD, TD, and ER2–ER4, and study the relationship between the upper and lower QPO frequencies as well as the corresponding resonance radii for frequency ratios of 1:1, 3:2, 4:3, and 5:4. Our results show that increasing α leads to deviations from the Schwarzschild case in both upper and lower QPO frequencies correlations and QPO orbital radii, with model-dependent trends. Further, we constrain the BH parameters using the observational data using MCMC analysis. Finally, we calculate the upper and lower QPO frequencies for a few BH candidates on the basis of the RP model using the constrained parameter values and find a good agreement with the observed results.

Keywords: Trace anomaly; Quantum gravity; Quasi periodic oscillation; Black holes

I. INTRODUCTION

General Relativity (GR) has been the most successful and extensively tested theory of gravity. Its predictions have been tested to a high precision through a wide range of experiments and astronomical observations. Among these, the recent detection of gravitational waves (GWs) by the LIGO collaboration [1–4] and the capturing of the image of black holes (BHs) by the Event Horizon Telescope (EHT) [6–11] are the major achievements in gravitational physics as well as in observational astrophysics. Despite these empirical successes, GR faces several profound theoretical challenges. Notably, it does not provide a satisfactory explanation for the accelerated expansion of the Universe, and it fails to explain the flat galaxy rotation curves obtained from observations, which are typically associated with dark energy and dark matter riddles, respectively [12–15]. Furthermore, GR is a classical theory and fails to incorporate quantum effects that are expected to dominate at high energy scales. In contrast, the Standard Model (SM) of particle physics [16, 17] is a very successful quantum theory of matters-radiation and their interactions which unifies the electromagnetic, weak, and strong interactions within the framework of Quantum Field Theory (QFT) [18, 19]. However, gravity remains excluded from this unification, primarily because GR is non-renormalizable and thus incompatible with the quantization procedures employed in QFT.

The unification of GR with the SM remains a central challenge in modern theoretical physics and continues to be an active area of research. In response to this challenge, several promising frameworks of Quantum Gravity (QG) have been developed to describe gravity within the framework of quantum physics. Among these most extensively studied approaches are Loop Quantum Gravity (LQG) [20–23] and String Theory [24–28]. LQG is developed within the framework of the Ashtekar formalism [29, 30] of GR, and it predicts that spacetime becomes discrete at extremely high energy scales. On the other hand, String Theory adopts a fundamentally different approach, proposing the existence of a boson particle known as the graviton, which acts as the mediator of the gravitational interaction.

Notwithstanding being the most extensively studied candidates for a theory of QG, both LQG and String Theory lack experimental validation. This problem arises because, to test the predictions of these theories, we require a very large amount of energy which is not currently achievable by existing experimental technologies. As a result, the direct empirical validation of these theories remains infeasible. Consequently, researchers have begun exploring alternative approaches to probe possible QG effects within more accessible energy regimes. One promising alternative is the Effective Field Theory (EFT) approach. EFT offers a framework to study the QG effects within an experimentally accessible energy scale, avoiding the need for ultra-high energies. In this formulation, GR is treated as a low-energy effective theory, valid up to a certain cutoff scale. This allows for the systematic inclusion of quantum corrections while preserving the agreement with classical GR in the low-energy regime. Numerous studies have been done in this approach, employing GR as an EFT to explore quantum gravitational phenomena (e.g. see [31–37]).

BHs are regions of spacetime where the gravitational field becomes so strong that not even light can escape. They represent one of the most fundamental and profound predictions of GR. Thus near a BH, gravity becomes extremely strong, and as a result, the small quantum effects arising from EFT corrections can become significant. The signatures of such effects can be observed

* Email: rupamjyotiborah856@gmail.com

† Email: umananda@dibru.ac.in

in different observables of BHs. Different properties of BHs, such as BH thermodynamics, quasinormal modes (QNMs), and BH shadows, have been extensively studied in this direction in the literature [48–55].

One of the significant quantum effects that naturally emerges in the EFT framework is the trace anomaly, also known as the conformal anomaly [56–58]. The classical field theories are conformally invariant and they exhibit a vanishing trace of the energy-momentum tensor. This symmetry is generally broken at the quantum level. In curved spacetime, this anomaly leads to a non-zero expectation value of the trace of the energy-momentum tensor. The trace anomaly captures the effects of quantum fields on the curvature of spacetime by adding specific geometric terms to the effective action. These terms depend on how spacetime is curved and include quantities like the square of the Weyl tensor, which measures the tidal distortion of spacetime, and the Gauss-Bonnet (GB) invariant, which combines different curvature components into a topological quantity. Together, these curvature dependent terms reflect how quantum corrections modify the classical description of gravity. These anomaly-induced corrections have profound implications for the semiclassical dynamics of spacetime, influencing phenomena like BH QNMs, [38, 39], quasi-periodic oscillations (QPOs) of BH [59–65], BH evaporation [40–42], quantum backreaction [43, 44], and early universe cosmology [45–47] etc. Within the EFT framework, the trace anomaly provides a concrete and calculable imprint of quantum effects in gravity, enabling theoretical predictions that remain compatible with the classical limit of GR. The effects of quantum corrections from EFT on gravity are typically very weak. However, they become significant in regions of extreme gravity, such as near the event horizon of a BH as mentioned earlier.

BH's QPOs are characteristic features observed in the X-ray light curves of accreting BH systems, especially in X-ray binaries. These oscillations appear as narrow peaks in the power density spectrum, indicating the presence of periodic or near-periodic modulations in the X-ray flux. QPOs are classified into two categories: low-frequency QPOs (LFQPOs) [66–68] and high-frequency QPOs (HFQPOs) [69, 70], based on their characteristic frequencies. QPOs are thought to originate from the innermost regions of the accretion disk, close to the event horizon, where strong gravity effects are significant. These frequencies are thought to correspond to fundamental modes of motion and are sensitive to the spacetime geometry surrounding the BH. Following their initial discovery via spectral and timing analyses in X-ray binaries [71], QPOs have been extensively investigated from both observational and theoretical perspectives [72–74, 80–82]. These efforts have led to the development of many theoretical works aiming to interpret the origin of QPOs within the framework of GR and accretion physics. A variety of models have been developed to capture the complex interplay between spacetime curvature, disk dynamics, and radiative processes in the vicinity of BHs [88–91]. These theoretical models aim to reproduce the observed QPO properties and their links to spectral states, which helps in the better understanding of the nature of the strong gravitational field near the BH. In spite of a large number of studies, the exact physical mechanisms responsible for generating QPOs remain an open question, with several competing models attempting to explain their origin. Continued advancements in observational techniques and theoretical modeling are essential to uncover the underlying physics driving these intriguing phenomena.

Thus, this study focuses on the effects of an EFT, which is based on the gravitational trace anomaly in GR, on the circular motion of a test particle around a BH and on the QPOs of the corresponding BH, and then constrains the parameters of the underlying theory using the QPO data. In Section II, we briefly discuss the BH solution in the presence of gravitational trace anomaly in GR. In Section III, we discuss the dynamics of a test particle around the BH in the said theory. In Section IV, we analyze the quasi-periodic and harmonic oscillations through the fundamental frequencies in this theoretical framework. The QPO models and QPO orbits for the BH influenced by trace anomaly have been studied in Section V. In Section VI, constraining the BH parameters using QPO data and MCMC analysis has been made. Finally, in Section VII, we summarize and conclude our work.

II. BLACK HOLE SOLUTIONS IN TRACE ANOMALY-INDUCED GRAVITY

As BHs are regions of spacetime where gravitational effects become extremely strong, studying BHs influenced by the gravitational trace anomaly therefore offers a powerful avenue for exploring the physical implications of quantum behaviours in curved spacetime. The gravitational theory with the trace anomaly was first introduced in Ref. [76] and the BHs incorporating the gravitational trace anomaly were first studied in Ref. [75]. This section provides a brief overview of the main steps involved in deriving the BH solution with the gravitational trace anomaly.

The gravitational action that avoids the problem of strong coupling in GR and is suitable for the quantum level is given by (see Refs. [75, 76])

$$S = S_{R\bar{R}} + S_A. \quad (1)$$

In this action (1) the first term $S_{R\bar{R}}$ is given as

$$S_{R\bar{R}} = M^2 \int d^4x \sqrt{-g} R - \bar{M}^2 \int d^4x \sqrt{-\bar{g}} \bar{R}, \quad (2)$$

where g is the determinant of the metric tensor $g_{\mu\nu}$ and \bar{g} is the determinant of $\bar{g}_{\mu\nu}$. The metric tensor $\bar{g}_{\mu\nu}$ is related to $g_{\mu\nu}$ by

the conformal transformation:

$$\bar{g}_{\mu\nu} = e^{-2\phi} g_{\mu\nu} \quad (3)$$

with ϕ identified as a massless scalar degree of freedom of the conformal field. R and \bar{R} are Ricci scalars evaluated in terms of $g_{\mu\nu}$ and $\bar{g}_{\mu\nu}$ respectively. M is a constant that is related to reduced Planck mass M_{pl} as $M = M_{pl}/\sqrt{2}$. \bar{M} is a new mass scale which is significantly smaller than M . The trace anomaly action S_A is expressed as [75]

$$S_A[\bar{g}, \phi] = \int d^4x \sqrt{-\bar{g}} [-\alpha (\phi \bar{\mathcal{G}} - 4\bar{G}^{\mu\nu} \bar{\nabla}_\mu \phi \bar{\nabla}_\nu \phi + 8\bar{X} \bar{\square} \phi - 8\bar{X}^2) + \beta \phi \bar{W}^2], \quad (4)$$

where α and β are the coupling parameters, $\bar{G}^{\mu\nu}$ is the conformally transformed Einstein tensor, $\bar{\mathcal{G}}$ and \bar{W}^2 respectively are the conformally transformed Gauss-Bonnet and square of Weyl terms, whose forms are $\bar{\mathcal{G}} = \bar{R}^2 - 4\bar{R}_{\mu\nu}\bar{R}^{\mu\nu} + \bar{R}_{\mu\nu\rho\sigma}\bar{R}^{\mu\nu\rho\sigma}$ and $\bar{W}^2 = \bar{R}^2/2 - 2\bar{R}_{\mu\nu}\bar{R}^{\mu\nu} + \bar{R}_{\mu\nu\rho\sigma}\bar{R}^{\mu\nu\rho\sigma}$ respectively. Further, \bar{X} can be express as $\bar{X} = -(1/2)\bar{g}^{\mu\nu}\bar{\nabla}_\mu\bar{\nabla}_\nu\phi$. Moreover, all the quantities with a bar in Eq. (4) are in the conformally transformed frame. Thus, the total action S in the conformally transformed frame can be represented as follows:

$$S = \int d^4x \sqrt{-\bar{g}} [M^2 e^{2\phi} (\bar{R} - 12\bar{X}) - \bar{M}^2 \bar{R} - \alpha (\phi \bar{\mathcal{G}} - 4\bar{G}^{\mu\nu} \bar{\nabla}_\mu \phi \bar{\nabla}_\nu \phi + 8\bar{X} \bar{\square} \phi - 8\bar{X}^2) + \beta \phi \bar{W}^2]. \quad (5)$$

The action with $\beta = 0$ i.e. action with only GB trace anomaly term is

$$S = \int d^4x \sqrt{-\bar{g}} [M^2 e^{2\phi} (\bar{R} - 12\bar{X}) - \bar{M}^2 \bar{R} - \alpha (\phi \bar{\mathcal{G}} - 4\bar{G}^{\mu\nu} \bar{\nabla}_\mu \phi \bar{\nabla}_\nu \phi + 8\bar{X} \bar{\square} \phi - 8\bar{X}^2)]. \quad (6)$$

In the conformally transformed frame with metric tensor $\bar{g}_{\mu\nu}$, if we consider a static and spherically symmetric spacetime, the line element can be expressed as

$$d\bar{s}^2 = -\bar{f}(\bar{r}) dt^2 + \frac{1}{\bar{h}(\bar{r})} d\bar{r}^2 + \bar{r}^2 (d\theta^2 + \sin^2 \theta d\varphi^2), \quad (7)$$

where $\bar{f}(\bar{r})$ and $\bar{h}(\bar{r})$ are the metric functions in the conformal frame. Also, it is assumed that the scalar field ϕ is a function of radial coordinate \bar{r} only, i.e. $\phi = \phi(\bar{r})$. The line element associated with the original frame with metric tensor $g_{\mu\nu} = e^{2\phi} \bar{g}_{\mu\nu}$ is

$$ds^2 = -f(r) dt^2 + \frac{1}{h(r)} dr^2 + r^2 (d\theta^2 + \sin^2 \theta d\varphi^2). \quad (8)$$

These two line elements are related by the transformation $d\bar{s}^2 = e^{-2\phi} ds^2$ and hence the temporal, radial and angular components of these two line elements are related as

$$f(r) = \bar{f}(\bar{r}) e^{2\phi}, \quad h(r) = \bar{h}(\bar{r}) [1 + \bar{r}\phi'(\bar{r})]^2, \quad r = \bar{r} e^\phi, \quad (9)$$

where $\phi'(\bar{r})$ is the derivative of $\phi(\bar{r})$ with respect to \bar{r} .

Upon evaluating the tt and $\bar{r}\bar{r}$ components of the field equations, which are obtained by the variation of action (1), we derive the following differential equations for $\bar{f}(\bar{r})$ and $\bar{h}(\bar{r})$ [75]:

$$\frac{\bar{f}'}{\bar{f}} = \frac{\bar{M}^2(\bar{h}-1) - M^2 e^{2\phi} [\bar{h}(3\bar{r}\phi' + 1)(\bar{r}\phi' + 1) - 1] - \alpha \bar{h}\phi'^2 [\bar{h}\{\bar{r}\phi'(3\bar{r}\phi' + 8) + 6\} - 2]}{\bar{h} [M^2 \bar{r}(\bar{r}\phi' + 1)e^{2\phi} + 2\alpha\phi'(\bar{h}\{3 + \bar{r}\phi'(\bar{r}\phi' + 3)\} - 1) - \bar{M}^2 \bar{r}]}, \quad (10)$$

$$\frac{\bar{h}'}{\bar{h}} - \frac{\bar{f}'}{\bar{f}} = \frac{2(\phi'^2 - \phi'') [M^2 \bar{r}^2 e^{2\phi} + 2\alpha(\bar{r}^2 \bar{h}\phi'^2 + 2\bar{r}\bar{h}\phi' + \bar{h} - 1)]}{\bar{r} M^2 e^{2\phi} (\bar{r}\phi' + 1) - \bar{r} \bar{M}^2 + 2\alpha\phi'(\bar{r}^2 \bar{h}\phi'^2 + 3\bar{r}\bar{h}\phi' + 3\bar{h} - 1)}. \quad (11)$$

Again, the variation of the action (1) with respect to ϕ in the frame with metric $g_{\mu\nu}$ yields [75]:

$$2M^2 R - \alpha \mathcal{G} + \beta W^2 = 0. \quad (12)$$

In the conformally transformed frame with metric $\bar{g}_{\mu\nu}$, Eq. (12) can be expressed as

$$2\bar{M}^2 \bar{R} - \alpha \bar{\mathcal{G}} + \beta \bar{W}^2 = 0. \quad (13)$$

From Eq. (13) we obtain,

$$\begin{aligned} & [2\bar{r}^2 \bar{f} \bar{h} \bar{f}'' - \bar{r} \bar{f}' (\bar{r} \bar{h} \bar{f}' - \bar{r} \bar{f} \bar{h}') - 4\bar{f} \bar{h}] + 4\bar{f}^2 (\bar{h} - 1) + 4\bar{r} \bar{f}^2 \bar{h}' \bar{M}^2 \\ & + 2\alpha [2\bar{f} \bar{h} (\bar{h} - 1) \bar{f}'' - \bar{f}' (\bar{h}^2 \bar{f}' - 3\bar{f} \bar{h} \bar{h}' - \bar{f}' \bar{h} + \bar{f} \bar{h}')] = 0. \end{aligned} \quad (14)$$

The general forms of the solutions for $\bar{f}(\bar{r})$, $\bar{h}(\bar{r})$ and $\bar{\phi}(\bar{r})$ under the Schwarzschild ansatz can be expressed as follows:

$$f(\bar{r}) = \left(1 - \frac{\bar{r}_h}{\bar{r}}\right) \left[1 + \sum_{i=1}^{\infty} \bar{f}_i(\bar{r}) \alpha^i\right], \quad h(\bar{r}) = \left(1 - \frac{\bar{r}_h}{\bar{r}}\right) \left[1 + \sum_{i=1}^{\infty} \bar{h}_i(\bar{r}) \alpha^i\right], \quad \phi(\bar{r}) = \phi_0 + \sum_{i=1}^{\infty} \phi_i(\bar{r}) \alpha^i. \quad (15)$$

Here, $\bar{f}_i(\bar{r})$, $\bar{h}_i(\bar{r})$ and $\phi_i(\bar{r})$ denote functions of the radial coordinate \bar{r} , and \bar{r}_h represents the event horizon radius of the BH in the barred frame. However, for consistency with the subsequent analysis performed in the unbarred coordinate system defined by $g_{\mu\nu}$, i.e., in the unbarred frame, we identify the physical event-horizon radius as $r_h = 2\mathcal{M}$, with \mathcal{M} being the mass of the BH. For validity of Eq. (15) requires the following condition to be fulfilled:

$$\frac{\alpha}{\bar{M}^2 \bar{r}_h^2} \ll 1. \quad (16)$$

Substituting Eq. (15) into Eqs. (10), (11) and (14), and solving the resulting differential equations, the BH solutions with scalar hair can be systematically derived at each order in α . The expressions for $\bar{f}(\bar{r})$, $\bar{h}(\bar{r})$ and $\bar{\phi}(\bar{r})$ up to the order of α^2 are given below [75]:

$$\begin{aligned} \bar{f}(\bar{r}) = & \left(1 - \frac{\bar{r}_h}{\bar{r}}\right) \left[1 + \frac{23\bar{r}^2 + 11\bar{r}_h\bar{r} + 6\bar{r}_h^2}{18\bar{M}^2 \bar{r}_h \bar{r}^3} \alpha - \frac{1}{32400\bar{M}^2 \bar{M}^4 \bar{r}_h^3 \bar{r}^6} \right. \\ & \times \left\{ \bar{M}^2 \left(38731\bar{r}^5 + 26371\bar{r}_h\bar{r}^4 + 22721\bar{r}_h^2\bar{r}^3 - 769\bar{r}_h^3\bar{r}^2 - 5572\bar{r}_h^4\bar{r} - 9300\bar{r}_h^5\right) e^{-2\phi_0} \right. \\ & \left. \left. - M^2 \left(6979\bar{r}^5 + 26539\bar{r}_h\bar{r}^4 + 28489\bar{r}_h^2\bar{r}^3 + 33379\bar{r}_h^3\bar{r}^2 + 13492\bar{r}_h^4\bar{r} + 4500\bar{r}_h^5\right) \right\} \alpha^2 + \mathcal{O}(\alpha^3) \right], \end{aligned} \quad (17)$$

$$\begin{aligned} \bar{h}(\bar{r}) = & \left(1 - \frac{\bar{r}_h}{\bar{r}}\right) \left[1 - \frac{(\bar{r} + 2\bar{r}_h)(\bar{r} + 5\bar{r}_h)}{18\bar{M}^2 \bar{r}_h \bar{r}^3} \alpha - \frac{1}{32400\bar{M}^2 \bar{M}^4 \bar{r}_h^3 \bar{r}^6} \right. \\ & \times \left\{ \bar{M}^2 \left(21211\bar{r}^5 + 13231\bar{r}_h\bar{r}^4 + 11041\bar{r}_h^2\bar{r}^3 - 33019\bar{r}_h^3\bar{r}^2 - 36964\bar{r}_h^4\bar{r} - 40300\bar{r}_h^5\right) e^{-2\phi_0} \right. \\ & \left. \left. + M^2 (\bar{r} - \bar{r}_h) \left(1901\bar{r}^4 - 4178\bar{r}_h\bar{r}^3 - 15747\bar{r}_h^2\bar{r}^2 - 4976\bar{r}_h^3\bar{r} - 1300\bar{r}_h^4\right) \right\} \alpha^2 + \mathcal{O}(\alpha^3) \right], \end{aligned} \quad (18)$$

$$\begin{aligned} \bar{\phi}(\bar{r}) = & \phi_0 - \frac{(6\bar{r}^2 + 3\bar{r}_h\bar{r} + 2\bar{r}_h^2)(M^2 - \bar{M}^2 e^{-2\phi_0})}{18\bar{M}^2 \bar{M}^2 \bar{r}_h \bar{r}^3} \alpha - \frac{1}{32400\bar{M}^4 \bar{M}^4 \bar{r}_h^3 \bar{r}^6} \\ & \times \left[3\bar{M}^4 (740\bar{r}^5 - 130\bar{r}_h\bar{r}^4 - 20\bar{r}_h^2\bar{r}^3 + 1285\bar{r}_h^3\bar{r}^2 + 6887\bar{r}_h^4\bar{r} + 300\bar{r}_h^5) \right. \\ & - 200\bar{M}^2 \bar{M}^2 e^{-2\phi_0} (33\bar{r}^5 + 18\bar{r}_h\bar{r}^4 + 16\bar{r}_h^2\bar{r}^3 + 33\bar{r}_h^3\bar{r}^2 + 15\bar{r}_h^4\bar{r} + 6\bar{r}_h^5) \\ & \left. + \bar{M}^4 e^{-4\phi_0} (4380\bar{r}^5 + 3990\bar{r}_h\bar{r}^4 + 3260\bar{r}_h^2\bar{r}^3 + 2745\bar{r}_h^3\bar{r}^2 + 936\bar{r}_h^4\bar{r} + 300\bar{r}_h^5) \right] \alpha^2 + \mathcal{O}(\alpha^3). \end{aligned} \quad (19)$$

Here, ϕ_0 is the asymptotic value of the scalar field $\phi(\bar{r})$ at spatial infinity. Moreover, it is to be noted that the metric functions $f(r)$ and $h(r)$ in the coordinate frame defined by the metric tensor $g_{\mu\nu}$ can be expressed in terms of the radial coordinate r by utilizing the correspondence relation given in Eq. (9). Thus by setting $\phi_0 = 0$, the resulting expressions for $f(r)$ and $h(r)$ are obtained from Eqs. (17) and (18) through the substitutions of $\bar{r} \rightarrow r$, $\bar{r}_h \rightarrow r_h$, $\bar{M} \rightarrow M$, and $M \rightarrow \bar{M}$, namely:

$$\begin{aligned} f(r) = & \left(1 - \frac{r_h}{r}\right) \left[1 + \frac{23r^2 + 11r_h r + 6r_h^2}{18M^2 r_h r^3} \alpha - \frac{1}{32400\bar{M}^2 M^4 r_h^3 r^6} \right. \\ & \times \left\{ M^2 \left(38731r^5 + 26371r_h r^4 + 22721r_h^2 r^3 - 769r_h^3 r^2 - 5572r_h^4 r - 9300r_h^5\right) \right. \\ & \left. \left. - \bar{M}^2 \left(6979r^5 + 26539r_h r^4 + 28489r_h^2 r^3 + 33379r_h^3 r^2 + 13492r_h^4 r + 4500r_h^5\right) \right\} \alpha^2 + \mathcal{O}(\alpha^3) \right], \end{aligned} \quad (20)$$

$$\begin{aligned}
h(r) = & \left(1 - \frac{r_h}{r}\right) \left[1 - \frac{(r+2r_h)(r+5r_h)}{18M^2 r_h r^3} \alpha - \frac{1}{32400 \bar{M}^2 M^4 r_h^3 r^6} \right. \\
& \times \left\{ M^2 \left(21211r^5 + 13231r_h r^4 + 11041r_h^2 r^3 - 33019r_h^3 r^2 - 36964r_h^4 r - 40300r_h^5 \right) \right. \\
& \left. \left. + \bar{M}^2 (r - r_h) \left(1901r^4 - 4178r_h r^3 - 15747r_h^2 r^2 - 4976r_h^3 r - 1300r_h^4 \right) \right\} \alpha^2 + \mathcal{O}(\alpha^3) \right]. \quad (21)
\end{aligned}$$

Thus, Eqs. (20) and (21) represent the black hole solutions in the presence of the GB trace anomaly, accurate up to second order in α . In the following sections, we will make use of these solutions for further investigations. It is to be noted here that in the underlying quantum theory, the coupling parameter α is proportional to the GB anomaly coefficient of the conformal matter field, which is non-negative for any unitary four-dimensional conformal field theory and is therefore non-negative in physically consistent anomaly-induced effective actions [77–79]. For this reason, and following the conventions of anomaly-induced effective actions, we restrict our analysis to $\alpha \geq 0$ in the present work.

III. PARTICLE MOTION AROUND BLACK HOLES MODIFIED BY TRACE ANOMALY

In this section, we investigate the motion of test particles under different conditions in the spacetime of BHs influenced by the GB trace anomaly. In all numerical computations, we work in geometrized units, $G = c = 1$. Following the standard practice in BH accretion and QPO studies, we express all radii and frequencies in units of the BH mass \mathcal{M} , so that these quantities become dimensionless. In practice, we set $\mathcal{M} = 1$ for all numerical calculations. Moreover, in the unbarred frame, the perturbative condition (16) takes the form $\alpha/M^2 r_h^2$, where M is the new mass scale appearing in the anomaly-induced action, related to the reduced Planck mass by $M = M_{\text{pl}}/\sqrt{2}$. In our analysis, we consider values of the anomaly parameter α of the order of 10^{-5} , and we identify the horizon radius as $r_h = 2\mathcal{M}$. Thus in the chosen unit of $\mathcal{M} = 1$ along with $M_{\text{pl}} = 1$, the value of $\alpha/M^2 r_h^2$ become the order of $\sim 10^{-5}$ in the explored parameter range. Since this is several orders of magnitude smaller than 1, the perturbative condition (16) will be safely satisfied throughout the entire parameter space used in this work.

A. Equations of Motion

The trajectories of test particles are determined by the following Lagrangian:

$$\mathcal{L}_p = \frac{1}{2} m g_{\mu\nu} u^\mu u^\nu, \quad (22)$$

where m is the mass and $u^\mu = dx^\mu/d\tau$ is the four velocity of a test particle. It is important to emphasize that $x^\mu(\tau)$ describes the particle's worldline, which is parametrized by the proper time τ . In a spherically symmetric spacetime, the underlying symmetries give rise to two Killing vectors: one is associated with time-translation invariance, $\xi^\mu = (1, 0, 0, 0)$, and the other corresponds to rotational symmetry about the azimuthal axis, $\eta^\mu = (0, 0, 0, 1)$. These symmetries imply the existence of conserved quantities along the particle's worldline. Specifically, they lead to the conservation of the test particle's total energy \mathcal{E} and angular momentum \mathcal{J} . These constants of motion can be expressed as

$$\mathcal{E} = -g_{tt} \dot{t} \quad \text{and} \quad \mathcal{J} = g_{\phi\phi} \dot{\phi}, \quad (23)$$

where the overdot represents differentiation with respect to proper time τ . The equation governing the motion of the test particle can be obtained by applying the following normalization condition [80]:

$$g_{\mu\nu} u^\mu u^\nu = \delta, \quad (24)$$

where $\delta = 0$ for massless particles and $\delta = \pm 1$ for massive particles with $\delta = +1$ for the spacelike geodesic of the particle and $\delta = -1$ for the timelike geodesic of the particle. Using the above condition (24) and considering the motion of the particle in the equatorial plane (i.e., $\theta = \pi/2$ and $\dot{\theta} = 0$), the equations of motion for the test particle around our considered BHs can be derived as

$$\dot{r}^2 = h(r) \left(\frac{\mathcal{E}^2}{f(r)} - \frac{\mathcal{J}^2}{r^2} - 1 \right), \quad (25)$$

$$\dot{\theta}^2 = 0, \quad \dot{\phi} = \frac{\mathcal{J}}{r^2}, \quad \dot{t} = \frac{\mathcal{E}}{f(r)}. \quad (26)$$

The radial equation of motion (25) in terms of coordinate time can be expressed in a Newtonian-like form (under the approximation $f(r) \approx h(r)$) as

$$\dot{r}^2 = \mathcal{E}^2 - V_{\text{eff}}, \quad (27)$$

where V_{eff} denotes the effective potential governing the radial motion in the equatorial plane, and it is given by

$$V_{\text{eff}} = h(r) \left(1 + \frac{\mathcal{J}^2}{r^2} \right). \quad (28)$$

Fig. 1 illustrates the variation of the effective potential V_{eff} for a test particle with respect to the radial coordinate normalized by the BH mass $r\mathcal{M}^{-1}$ and for different values of the GB coupling constant α . It should be noted that the values of α , \bar{M} , and M have been chosen to satisfy the condition (16). It is evident from Fig. 1 that the peak of the effective potential V_{eff} increases with

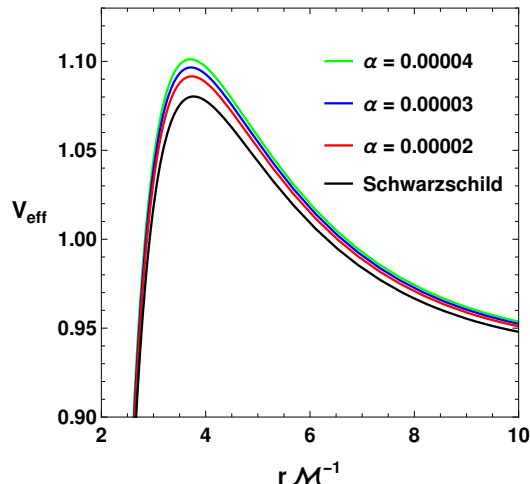


FIG. 1. Variation of the effective potential (28) with radial coordinate normalized by the BH mass $r\mathcal{M}^{-1}$ for different values of α . Here we consider $\bar{M} = 0.003$.

increasing values of the GB coupling constant α , which is higher for all values of α as compared to the Schwarzschild BH case. It is to be noted here that in all our numerical calculations we consider $M_{pl} = 1$ and hence $M = 1/\sqrt{2}$.

B. Circular Orbits

In this subsection, we explore the circular motion of test particles around the BHs by imposing the following conditions [80, 81]:

$$\dot{r} = 0 (V_{\text{eff}} = \mathcal{E}^2) \text{ and } V'_{\text{eff}} = 0, \quad (29)$$

where the prime indicates the derivative with respect to the radial coordinate r . The condition $V'_{\text{eff}} = 0$ identifies the stationary points of the effective potential, which correspond to circular orbits. The requirement that these points be minima ensures the stability of the orbits, such that small perturbations will keep the particle bound to its circular path. Using these conditions, we derive the expressions for the energy and angular momentum of the particle, which are provided in the Appendix. In Fig. 2, we plot the specific energy \mathcal{E} and specific angular momentum \mathcal{J} (not their squared values). Both quantities \mathcal{E} and \mathcal{J} are in the unit normalised by the BH mass \mathcal{M} . This figure depicts the radial dependence of specific angular momentum and energy of the particle. The left panel shows the variation of the specific angular momentum with respect to $r\mathcal{M}^{-1}$. With the increase in the value of α , the minimum of the angular momentum shifts to lower values compared to the Schwarzschild BH. The middle panel shows the variation of the energy \mathcal{E} , with respect to $r\mathcal{M}^{-1}$. In this case also with an increase in the value of the GB trace anomaly coupling constant α , the minimum of the energy shifts to lower values compared to the Schwarzschild BH. The minimum in the energy profile corresponds to the most stable circular orbit. The right panel depicts the variation of the specific energy \mathcal{E} with specific angular momentum \mathcal{J} . As α increases, the curves shift, leading to a decrease in the required angular momentum for a given energy. Compared to the Schwarzschild case, the presence of the trace anomaly allows circular orbits with lower angular momentum for the same energy, highlighting the influence of the GB trace anomaly on particle dynamics near BHs.

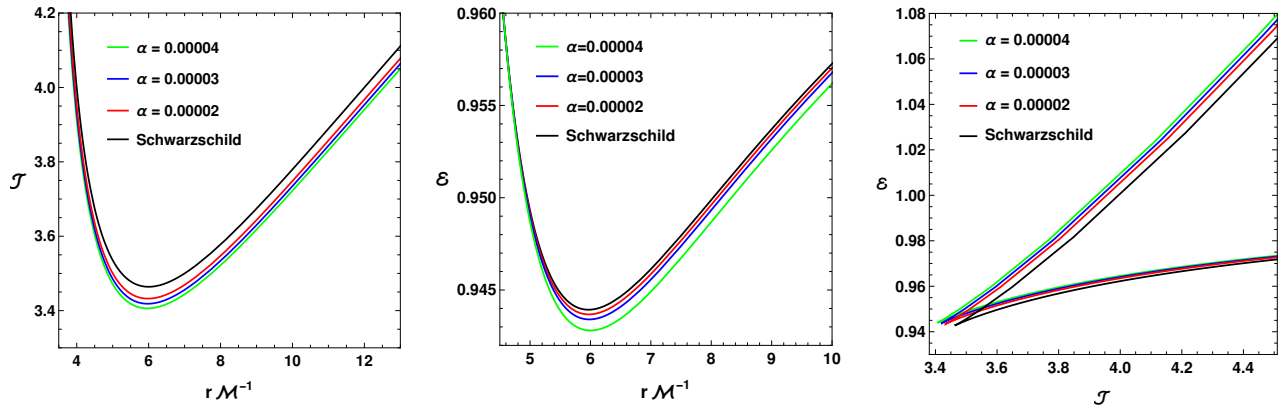


FIG. 2. Radial profiles of specific angular momentum and energy for circular orbits of test particles are shown for different values of α , obtained by considering $\bar{M} = 0.003$.

C. Innermost Stable Circular Orbits

The stable circular orbits for a test particle around a BH exist at a specific radius, denoted by $r = r_{\min}$, which corresponds to the point where the particle possesses the least possible energy and angular momentum required to maintain a circular trajectory. This particular radius represents an energetically favorable position for the particle's motion. When considering the innermost stable circular orbit (ISCO), an additional criterion must be met to ensure the stability of the orbit against small perturbations. Specifically, the effective potential V_{eff} governing the radial motion of the particle must satisfy the conditions that both the first and second derivatives of its must vanish, i.e., $V'_{\text{eff}} = 0$ and $V''_{\text{eff}} = 0$. These two conditions together determine the precise location of the ISCO, ensuring that the orbit is not only circular but also marginally stable. Since the expression for the effective potential in our chosen BH system involves complicated mathematical terms, we used numerical methods to determine the ISCO radius. The variation of the ISCO radius with respect to the GB coupling constant α is then plotted for different values of the parameter \bar{M} . Fig. 3 illustrates the variation of the ISCO radius normalized by the BH mass with respect to α . It is observed that as α

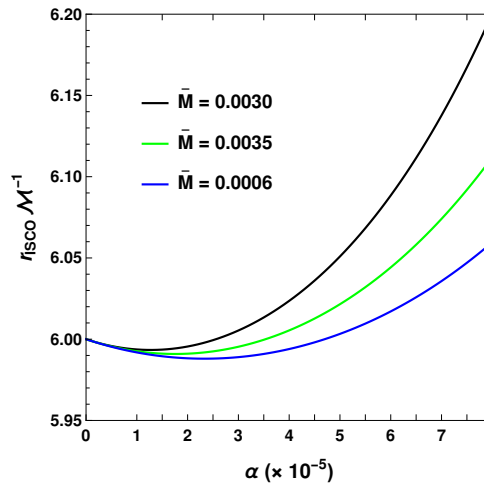


FIG. 3. Variation of the ISCO radius normalized by the BH mass \mathcal{M} with respect to GB coupling constant α for different values of \bar{M} .

increases, the ISCO radius also increases for all chosen values of \bar{M} . This trend suggests that the effect of the GB trace anomaly is to push the stable circular orbits outward, causing particles to orbit at relatively larger radii as α grows. Additionally, for higher values of \bar{M} , the ISCO radius is consistently larger, indicating that both α and \bar{M} contribute to shifting the ISCO outward. This behavior reflects the impact of higher-curvature corrections on the geodesic structure of the BH spacetime.

IV. FUNDAMENTAL FREQUENCIES

In this section, we derive the analytical expressions for the fundamental frequencies associated with the motion of test particles around BHs influenced by the GB trace anomaly. These frequencies are essential for characterizing small perturbative oscillations about circular geodesics in the BH spacetime. Such oscillations provide a theoretical basis for interpreting QPOs observed in the X-ray flux of accreting compact objects. The study of these fundamental frequencies, specifically the orbital (Keplerian), radial epicyclic, and vertical epicyclic modes, serves as a powerful diagnostic tool to probe the nature of strong-field gravity near the event horizon. Within the framework of GB trace anomaly gravity, which introduces quantum corrections via a trace anomaly term in the effective gravitational action, deviations from GR are naturally incorporated. Consequently, analyzing these oscillation modes in the modified geometry offers a pathway to constrain the anomaly coupling parameter.

A. Keplerian Frequencies

The Keplerian frequency refers to the rate at which a test particle moves around a BH, as measured by an observer located far from the gravitational source. It is commonly represented by Ω_ϕ , and is defined as the ratio of the change in the azimuthal coordinate to the change in coordinate time, i.e., $\Omega_\phi = d\phi/dt$. Based on this definition, a general formula for the orbital or Keplerian frequency can be obtained in the context of a static and spherically symmetric spacetime geometry as follows [82]:

$$\Omega_\phi = \sqrt{\frac{-\partial_r g_{tt}}{\partial_r g_{\phi\phi}}} = \sqrt{\frac{f'(r)}{2r}}. \quad (30)$$

The Keplerian frequency for the Schwarzschild BH has the following form [80]:

$$\Omega_\phi = \sqrt{\frac{\mathcal{M}}{r^3}}. \quad (31)$$

We derive the Keplerian frequency Ω_ϕ for the BHs endowed with GB trace anomaly, as presented in Eq. (A.4) in the appendix. Taking the limit $\alpha \rightarrow 0$ in Eq. (A.4), we recover the result given in Eq. (31). Fig. 4 illustrates the variation of the Keplerian frequency, normalized by the BH mass \mathcal{M} , as a function of the normalized radial coordinate $r\mathcal{M}^{-1}$. It is evident from Fig. 4 that the magnitude of the Keplerian frequency $\Omega_\phi\mathcal{M}^{-1}$ decreases monotonically with increasing $r\mathcal{M}^{-1}$, as expected for circular orbits around a BH. When the GB trace anomaly correction is included, the resulting frequency profiles remain very close to the Schwarzschild curve for $r\mathcal{M}^{-1} > r_h\mathcal{M}^{-1}$ ($r_h\mathcal{M}^{-1} = 2$ in our case). This behaviour reflects the fact that the anomaly induced modification to the metric is a small perturbation that falls off rapidly with radius.

To express the angular frequency in terms of the physical frequency measured in Hertz (Hz), we use the relation as given by

$$\nu_\phi = \frac{1}{2\pi} \frac{c^3}{G\mathcal{M}} \Omega_\phi \text{ [Hz]}. \quad (32)$$

To convert the frequencies from the geometrized units to Hertz in the International System of Units (SI), we use the speed of light in vacuum, $c = 3 \times 10^8 \text{ ms}^{-1}$, and the gravitational constant, $G = 6.67 \times 10^{-11} \text{ m}^3 \text{ kg}^{-1} \text{ s}^{-2}$.

B. Harmonic Oscillations

In this subsection, we investigate the fundamental frequencies associated with the oscillatory motion of test particles around the BHs influenced by the GB trace anomaly. These fundamental frequencies, corresponding to radial and vertical oscillations, are determined by introducing small perturbations to the circular motion of the particles, especially by considering deviations of the form: $r \rightarrow r_0 + \delta r$ for radial perturbations and $\theta \rightarrow \theta_0 + \delta\theta$ for vertical perturbations. To facilitate this analysis, the effective potential is expanded in terms of r and θ around the equilibrium circular orbit as follows:

$$\begin{aligned} V_{\text{eff}}(r, \theta) = & V_{\text{eff}}(r_0, \theta_0) + \delta r \left. \frac{\partial V_{\text{eff}}(r, \theta)}{\partial r} \right|_{r_0, \theta_0} + \delta\theta \left. \frac{\partial V_{\text{eff}}(r, \theta)}{\partial \theta} \right|_{r_0, \theta_0} + \frac{1}{2} \delta r^2 \left. \frac{\partial^2 V_{\text{eff}}(r, \theta)}{\partial r^2} \right|_{r_0, \theta_0} \\ & + \frac{1}{2} \delta\theta^2 \left. \frac{\partial^2 V_{\text{eff}}(r, \theta)}{\partial \theta^2} \right|_{r_0, \theta_0} + \delta r \delta\theta \left. \frac{\partial^2 V_{\text{eff}}(r, \theta)}{\partial r \partial \theta} \right|_{r_0, \theta_0} + \mathcal{O}(\delta r^3, \delta\theta^3). \end{aligned} \quad (33)$$

By enforcing the conditions for circular motion and its stability, the expansion of the effective potential simplifies such that only the second-order derivative terms contribute to the dynamics. As a result, the radial and vertical perturbations reduce to equations

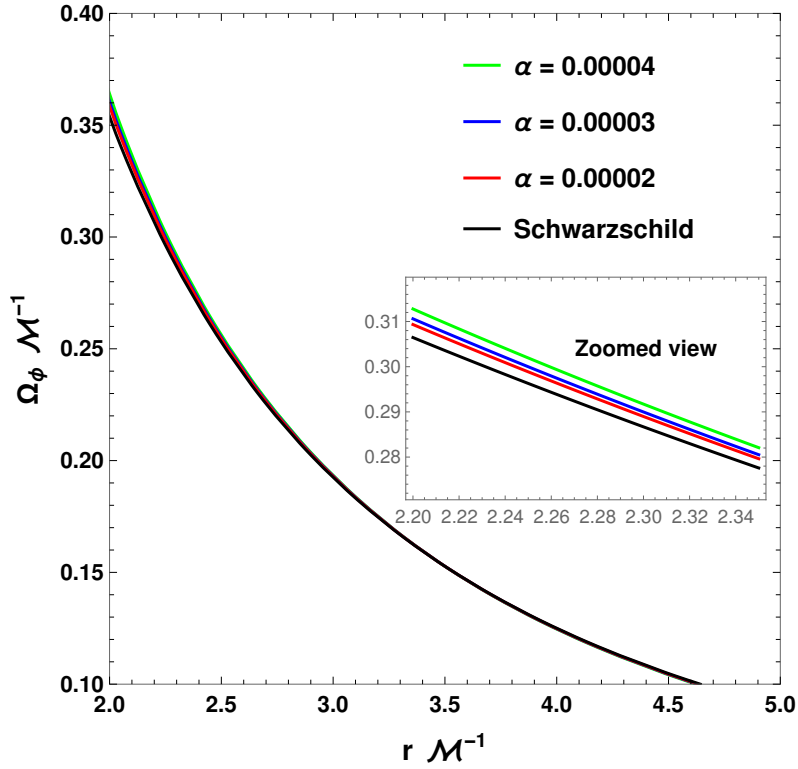


FIG. 4. Variation of $\Omega_\phi \mathcal{M}^{-1}$ with respect to $r \mathcal{M}^{-1}$ for different values of α obtained by considering $\bar{M} = 0.003$.

of harmonic oscillators in the equatorial plane. Consequently, these perturbations give rise to characteristic frequencies, which correspond to observable quantities for a distant observer. The forms of the reduced harmonic oscillator equations are as follows [80]:

$$\frac{d^2 \delta r}{dt^2} + \Omega_r^2 \delta r = 0, \quad \frac{d^2 \delta \theta}{dt^2} + \Omega_\theta^2 \delta \theta = 0, \quad (24)$$

where Ω_r and Ω_θ respectively, are the radial and vertical oscillation frequencies and can be express as follows:

$$\Omega_r^2 = -\frac{1}{2g_{rr}i^2} \partial_r^2 V_{\text{eff}}(r, \theta)|_{\theta=\pi/2}, \quad (34)$$

$$\Omega_\theta^2 = -\frac{1}{2g_{\theta\theta}i^2} \partial_\theta^2 V_{\text{eff}}(r, \theta)|_{\theta=\pi/2}. \quad (35)$$

For the BHs under consideration, the expressions for the radial and vertical frequencies are given by Eqs. (A.3) and (A.4) respectively in the appendix. These frequencies can be expressed in terms of physical frequencies measured in Hertz using the relation (32) by generalising Ω_ϕ and ν_ϕ as Ω_i and ν_i , where i stands for both r and θ as well as ϕ .

V. QPO MODELS AND QPO ORBITS IN BLACK HOLES

A. QPO models

This subsection investigates the possible frequencies of twin-peak QPOs in the spacetime of BHs influenced by the GB trace anomaly, providing a comparison with the corresponding results for standard Schwarzschild BHs across various QPO models. We present the forms of the upper (ν_U) and lower (ν_L) QPO frequencies in terms of ν_r , ν_θ and ν_ϕ , formulated according to each specific QPO model under consideration [83]. For instance, we adopt the following commonly used models.

1. Parametric Resonance (PR) Model

The frequent detection of a 3:2 ratio in twin-peak high-frequency QPOs from BH and neutron star systems has motivated the proposal that these oscillations may originate from nonlinear resonances between different modes of motion in the accretion disk [83–85]. In its simplest formulation, small perturbations in the radial and vertical directions around circular, equatorial geodesics are treated as independent harmonic oscillations, characterized by the radial (v_r) and vertical (v_θ) epicyclic frequencies, respectively. The PR model posits that radial oscillations, typically stronger than their vertical counterparts due to $\delta r > \delta \theta$ in thin accretion disks, can parametrically excite vertical oscillations when a specific resonance condition is met, given by $v_r/v_\theta = 2/n$, where n is a positive integer. In the case of rotating BHs, where $v_\theta > v_r$ generally holds, the resonance is strongest for $n = 3$, naturally leading to the frequently observed 3:2 frequency ratio. Within this framework, the upper and lower QPO frequencies are identified as $\nu_U = \nu_\theta$ and $\nu_L = \nu_r$, respectively.

2. Relativistic Precession (RP) model

In the RP model, QPOs in X-ray binaries are interpreted as a natural consequence of matter orbiting in the curved spacetime around compact objects. Here, plasma blobs in the accretion disk follow slightly eccentric and inclined geodesic orbits near the BHs, giving rise to distinct frequencies. According to this model, the upper kHz QPO corresponds to the Keplerian frequency, given by $\nu_U = \nu_\phi$, while the lower kHz QPO is associated with the periastron precession frequency, which is given by $\nu_L = \nu_\phi - \nu_r$. Additionally, low-frequency QPO frequencies are linked to nodal precession, given by $\nu_\phi - \nu_\theta$, related to vertical oscillations and frame dragging. This nodal frequency vanishes in the Schwarzschild case as in the Schwarzschild case $\nu_\phi = \nu_\theta$. These frequency identifications are strongly supported by general relativistic corrections to orbital motion, including effects of frame dragging and spacetime curvature, which naturally give rise to the observed precessional phenomena. Furthermore, the detection of harmonic structures in both neutron star and BH systems reinforces this interpretation, particularly in cases where even harmonics of the nodal precession frequency dominate the observed power spectrum [86–88]. The RP model provides a relativistic, geometrical explanation for QPOs, without invoking resonance mechanisms or magnetic fields.

3. Warped Disk (WD) model

The WD model explains high-frequency QPOs by considering a non-standard, warped geometry of the accretion disk [89, 90]. In this framework, nonlinear resonances occur between the warped structure of the disk and its intrinsic oscillation modes. These resonances involve interactions in both horizontal and vertical directions. The horizontal resonances can excite both g-mode and p-mode oscillations, whereas vertical resonances typically excite only g-modes. The emergence of these resonances is attributed to the non-monotonic variation of the radial epicyclic frequency with respect to the radial coordinate r . According to this model, the observed high-frequency QPOs are associated with the relations $\nu_U = 2\nu_\phi - \nu_r$ and $\nu_L = 2(\nu_\phi - \nu_r)$.

4. Tidal Disruption (TD) Model

The TD model interprets QPOs as a consequence of the tidal breakup of inhomogeneities, such as dense clumps of matter or external bodies, in the strong gravitational field of a BH. According to this model, the observed QPO frequencies are linked to the fundamental orbital frequencies of the disrupted material. Specifically, the upper frequency is identified as $\nu_U = \nu_\phi + \nu_r$, while the lower frequency corresponds to $\nu_L = \nu_\phi$. The TD model has been motivated by numerical simulations of tidal disruption events, where compact objects such as asteroids or stars are torn apart by the BH tidal forces. These simulations reveal the formation of a transient, bright, ring-like structure featuring an orbiting radiating core. This dynamically evolving configuration can naturally give rise to QPOs through the superposition of the orbital and epicyclic motions of the disrupted material. Thus, the TD model offers a physically motivated, relativistic mechanism for QPO generation based on the extreme tidal interactions near BHs [83, 91].

5. ER2, ER3, and ER4 Models

The epicyclic resonance (ER) model offers a relativistic framework for interpreting high-frequency QPOs as the result of nonlinear resonances between the fundamental oscillation modes of accreting matter in the vicinity of compact objects. In this scenario, QPOs arise due to resonances between the radial and vertical epicyclic frequencies of particles orbiting along slightly perturbed geodesic trajectories in a relativistic accretion disk. In this work, we specifically focus on three representative cases

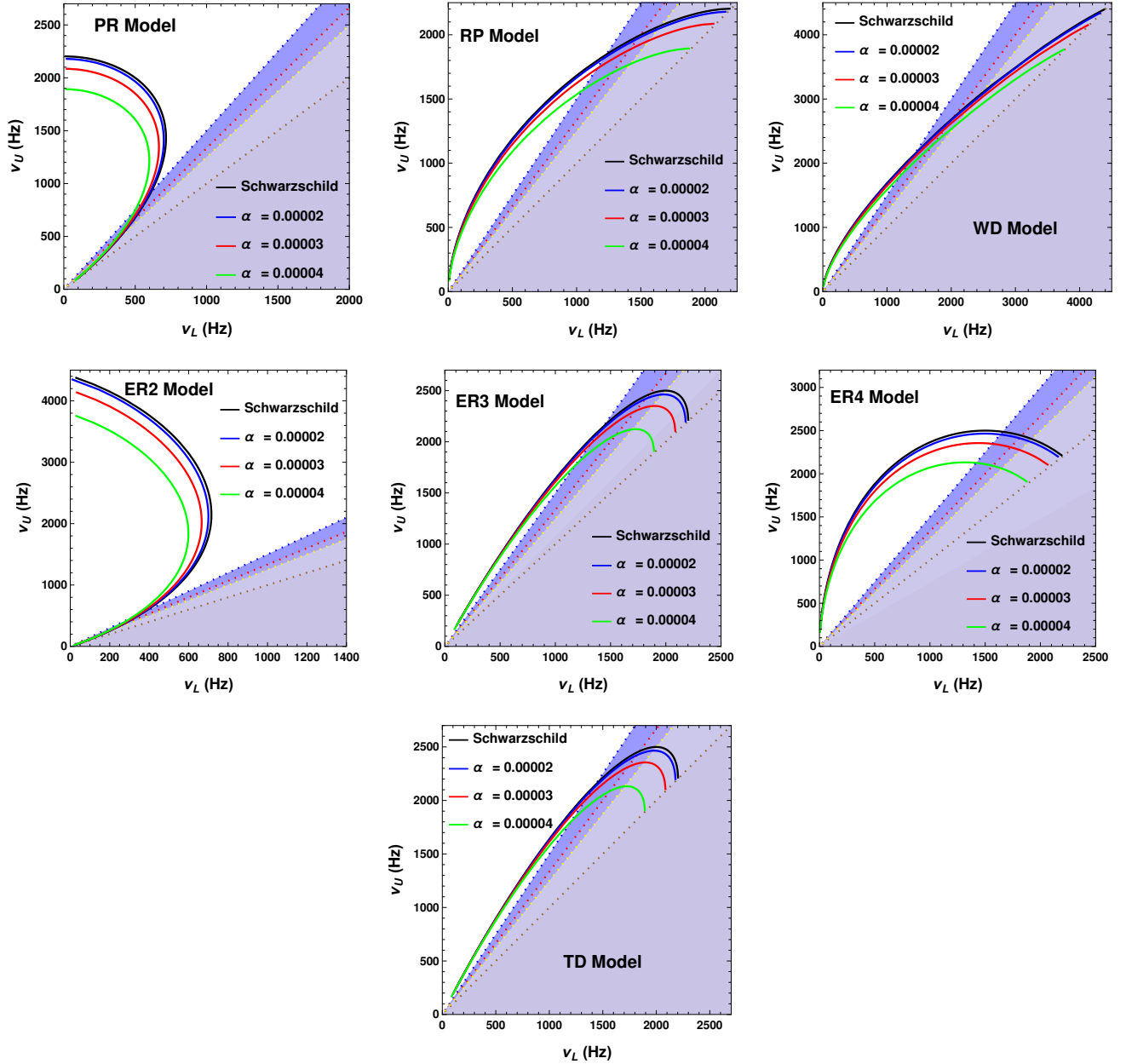


FIG. 5. Correlations between the upper (v_U) and lower (v_L) frequencies of twin-peak QPOs for different values of the coupling constant α as predicted by different QPO models mentioned in the text. In this analysis, we consider $\bar{M} = 0.003$ as a fixed parameter value.

of the ER model, viz., ER2, ER3, and ER4, each characterized by distinct combinations of the orbital and epicyclic frequencies. The QPO frequencies for these models are defined as follows [80]:

- For ER2, the upper and lower QPO frequencies are given by $v_U = 2v_\theta - v_r$ and $v_L = v_r$.
- For ER3, they are expressed as $v_U = v_\theta + v_r$ and $v_L = v_\theta$.
- For ER4, the relations take the form: $v_U = v_\theta + v_r$ and $v_L = v_\theta - v_r$.

Fig. 5 shows the relationship between the computed values of v_U and v_L for the considered BH spacetime, evaluated using the PR, RP, WD, TD, and ER2–ER4 models for different values of the GB coupling constant α . The diagram includes characteristic reference lines corresponding to the frequency ratios 3:2, 4:3, 5:4, and 1:1 between the upper and lower frequencies. Specifically, the 3:2 ratio is represented by a dotted blue line, 4:3 by a dotted red line, 5:4 by a dotted yellow line, and 1:1 by a dotted brown line. In addition, the plot shows shaded regions between these reference lines, visually highlighting distinct frequency ratio bands for the twin-peak QPOs. The line corresponding to the 1:1 frequency ratio is commonly referred to as the QPO

graveyard, as any QPO located on this line indicates the merging of the upper and lower frequencies into a single oscillation, effectively erasing the characteristic twin-peak structure. Fig. 5 clearly illustrates that as the GB coupling constant α increases, the predicted relationship between the upper and lower QPO frequencies progressively departs from the Schwarzschild reference curve, emphasizing the impact of the GB trace anomaly on the QPO characteristics.

B. QPO Orbits

In this subsection, we explore the influence of the GB coupling constant α on the orbital radii associated with QPOs, particularly those characterized by frequency ratios 1:1, 3:2, 4:3, and 5:4. These characteristic radii can be determined by satisfying the resonance condition [80]:

$$av_U(\mathcal{M}, r, \alpha) = bv_L(\mathcal{M}, r, \alpha), \quad (36)$$

where a and b are integers that define the specific resonance ratio, and v_U, v_L represent the upper and lower QPO frequencies respectively, as mentioned already. This condition is solved numerically for the radial coordinate $r\mathcal{M}^{-1}$ across various values of the GB parameter α , within the frameworks of the QPO models: PR, RP, WD, TD and ER2–ER4. The resulting solutions for $r\mathcal{M}^{-1}$ are presented in Fig. 6, which illustrates how the resonance locations evolve as a function of the coupling constant α . Fig. 6 displays the dependence of the QPO-generating orbital radii expressed in the unit of \mathcal{M} on the GB coupling constant α for all seven QPO models considered: PR, RP, WD, ER2, ER3, ER4, and TD. Each panel corresponds to a specific model and presents the orbital locations associated with the resonant frequency ratios 1:1, 3:2, 4:3, and 5:4, along with the ISCO. The plots reveal that the ER3 and TD models yield QPOs at significantly larger orbital radii compared to the other models, indicating the most extended resonance region among those models. This is followed by the ER2 and PR models, which also predict large resonance radii. In contrast, the RP model consistently produces the smallest QPO orbital radii. Furthermore, a consistent trend is observed across all models that the QPOs generating radii increase monotonically with the GB coupling parameter α , suggesting that the presence of the GB correction modifies the underlying spacetime geometry.

VI. MONTE CARLO MARKOV CHAIN ANALYSIS

In this section, we employ the Markov Chain Monte Carlo (MCMC) technique to place constraints on the parameters of our chosen BH system, using observational data from six prominent sources that span three distinct mass scales. These include four stellar-mass BH: GRO J1655–40, XTE J1550–564, GRS 1915+105, and H 1743–322, one intermediate-mass BH, M82 X-1, and the supermassive BH Sgr A*. A concise summary of these BH sources along with their corresponding observational characteristics is provided in Table I [92–102]. In this work, we use the RP model as a representative case to constrain the BH parameters by performing an MCMC analysis on these six BHs.

TABLE I. Mass and QPO frequencies of selected BH sources.

BH	Mass (in M_\odot)	Upper Frequency (Hz)	Lower Frequency (Hz)
GRO J1655–40	5.4 ± 0.3	441 ± 2	298 ± 4
XTE J1550–564	9.1 ± 0.61	276 ± 3	184 ± 5
GRS 1915+105	$12.4^{+2.0}_{-1.8}$	168 ± 3	113 ± 5
H 1743+322	$8.0 - 14.07$	242 ± 3	166 ± 5
M82 X-1	415 ± 63	5.07 ± 0.06	3.32 ± 0.06
Sgr A*	$(3.5 - 4.9) \times 10^6$	$(1.445 \pm 0.16) \times 10^{-3}$	$(0.886 \pm 0.04) \times 10^{-3}$

In order to get meaningful constraints on the model parameters, we use a Bayesian statistical framework. This approach allows us to incorporate prior knowledge and observational data in a consistent manner using the MCMC technique. The Bayesian posterior distribution is given by [103, 104]

$$P(\theta|D, \mathcal{T}_m) = \frac{P(D|\theta, \mathcal{T}_m)\pi(\theta|\mathcal{T}_m)}{P(D|\mathcal{T}_m)}, \quad (37)$$

where θ is the set of parameters in the model, i.e., $\theta = (\mathcal{M}, \bar{M}, \alpha, r\mathcal{M}^{-1})$ for our case, D is the observed data, \mathcal{T}_m denotes the theoretical model, $P(D|\theta, \mathcal{T}_m)$ is the likelihood function, which measures how well the model with parameters θ predicts the

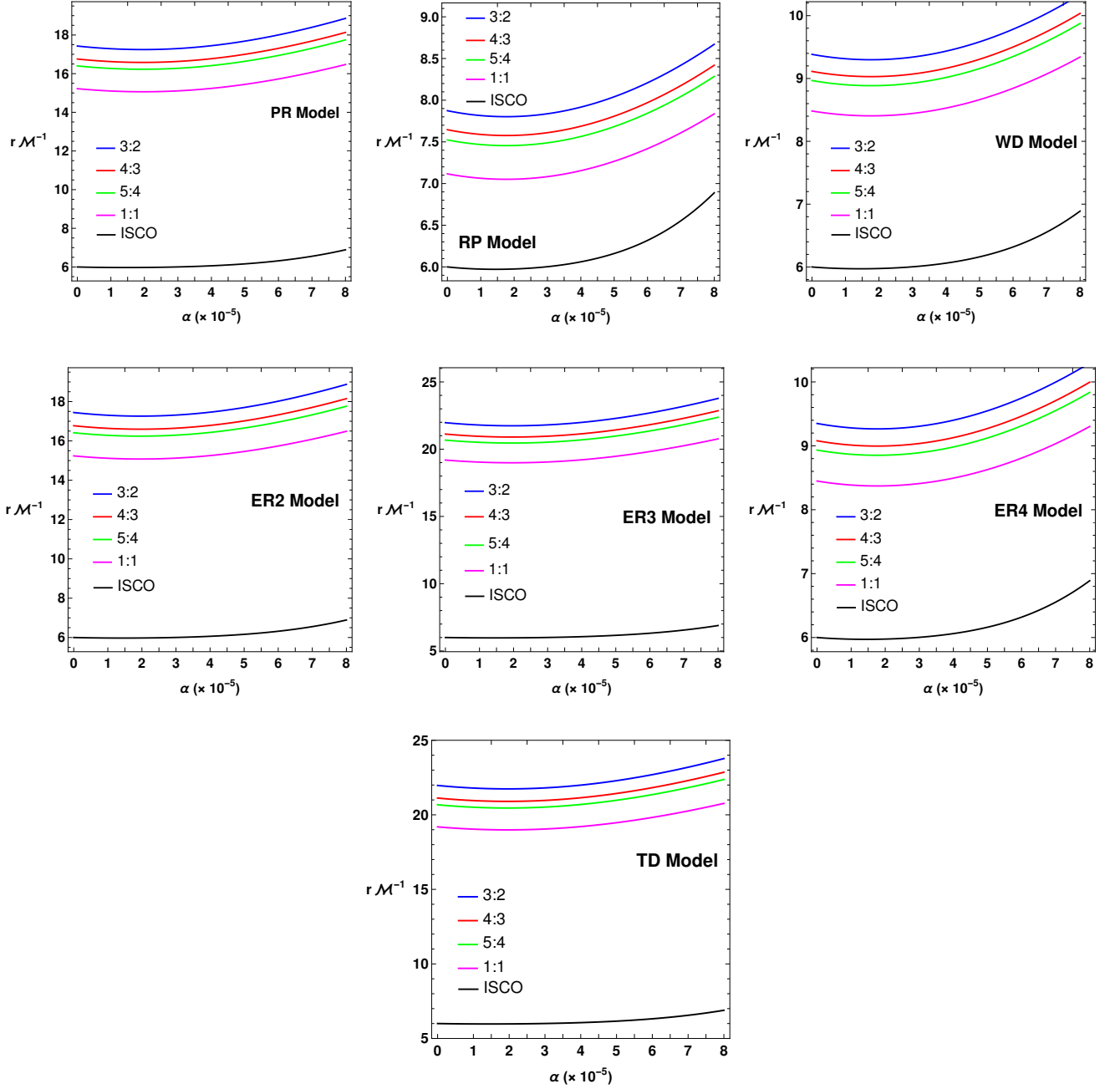


FIG. 6. Dependence of the QPO orbital radius on the GB coupling constant α for PR, RP, WD, ER2, ER3, ER4 and TD models.

observed data D , $\pi(\theta|\mathcal{T}_m)$ represents the prior distribution and $P(D|\mathcal{T}_m)$ is the marginal likelihood, which is a normalization factor ensuring the total probability over all θ sums to 1. A Gaussian prior can be defined as

$$\pi(\theta_i) \exp \left[-\frac{1}{2} \left(\frac{\theta_i - \theta_{0,i}}{\sigma_i} \right)^2 \right], \quad \theta_{low,i} < \theta_i < \theta_{high,i}, \quad (38)$$

where $\theta_i = (\mathcal{M}, \bar{M}, \alpha, r_i \mathcal{M}^{-1})$, $\theta_{0,i}$ is the mean and σ_i are the deviations of the corresponding parameters. In this work, we consider the priors to have Gaussian distributions.

The log-likelihood function is defined as the natural logarithm of the likelihood function. In the present case, it can be expressed as

$$\log P = \log P_U + \log P_L. \quad (39)$$

Here, $\log P_U$ is the log-likelihood of upper frequency and $\log P_L$ is the log-likelihood of lower frequency. These two likelihoods can be expressed as follows:

$$\log P_U = -\frac{1}{2} \sum_i \frac{(v_{\phi,obs}^i - v_{\phi,th}^i)^2}{(\sigma_{\phi,obs}^i)^2}, \quad (40)$$

$$\log P_L = -\frac{1}{2} \sum_i \frac{(v_{L,obs}^i - v_{L,th}^i)^2}{(\sigma_{L,obs}^i)^2}. \quad (41)$$

The quantities $v_{\phi,obs}$ and $v_{L,obs}$ represent the observed values of the orbital (Keplerian) frequency and the periastron precession (lower) frequency, respectively, for the astrophysical source under consideration. The lower frequency v_L is calculated as the difference between the Keplerian frequency v_{ϕ} and the radial epicyclic frequency v_r . Correspondingly, $v_{\phi,th}$ and $v_{L,th}$ denote the theoretical predictions for these frequencies based on the chosen model.

We then carry out an MCMC analysis to estimate the parameters of our chosen BHs. For this, we use known values from earlier QPO studies as a guide. For each parameter, we generate around 10^5 samples from its respective Gaussian prior. This approach enables a thorough exploration of the physically relevant parameter space and helps in determining the most suitable parameter values. Figs. 7 – 9 present the results of the MCMC analysis for six different BH systems. The left plot of Fig. 7

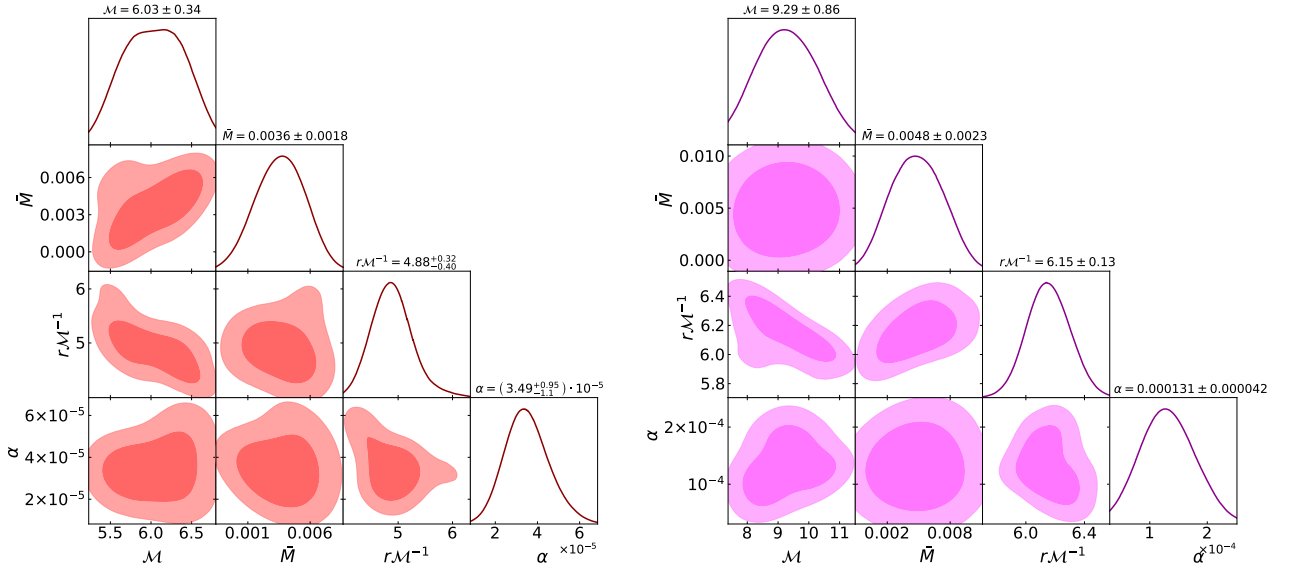


FIG. 7. MCMC outputs, showing the constraints on the parameters \mathcal{M} , \bar{M} , $r\mathcal{M}^{-1}$ and α , using data from GRO J1655–40 (left) and XTE J1550–564 (right) BHs.

corresponds to the GRO J1655–40 system, using its measured mass along with the upper and lower QPO frequencies. Similarly, the right plot of this figure displays results for the XTE J1550–564 BH, based on the same set of observational data. The left plot Fig. 8 corresponds to the BH GRS 1915+105 and its right plot corresponds to the BH system H 1743+322. Similarly, the left plot of Fig. 9 is based on the data from the BH M82 X-1, and the right plot of it uses data from the BH Sgr A*. In this analysis, the contour plots illustrate the confidence intervals of the posterior probability distributions for all the parameters, showing levels of 68% (1σ) and 95% (2σ). The shaded areas within the contours represent these respective confidence regions. The dark shaded region is for 1σ confidence interval and the light shaded region is for 2σ confidence interval. Table II shows the constraints on the model parameters for six different BHs. From Table II, it can be observed that the constrained values of \mathcal{M} are in good agreement with the available observational results, which shows the reliability of our analysis. For the parameter \bar{M} , the highest value is obtained for the BH system H 1743+322, while the lowest value corresponds to GRO J1655–40. In the case of the parameter α , we find the maximum value for GRS 1915+105 and the minimum for Sgr A*. These variations in the parameters indicate their source dependence. Finally, we calculated the theoretical values of the upper and lower QPO frequencies using the constrained parameters for all the BH systems listed in Table I, and the corresponding results are presented in Table III. In Table III, we also present the deviations of the theoretically calculated QPO frequencies from the observed values, computed using the following formula:

$$\Delta v (\%) = \left| \frac{v_{ob} - v_{th}}{v_{ob}} \right| \times 100\%, \quad (42)$$

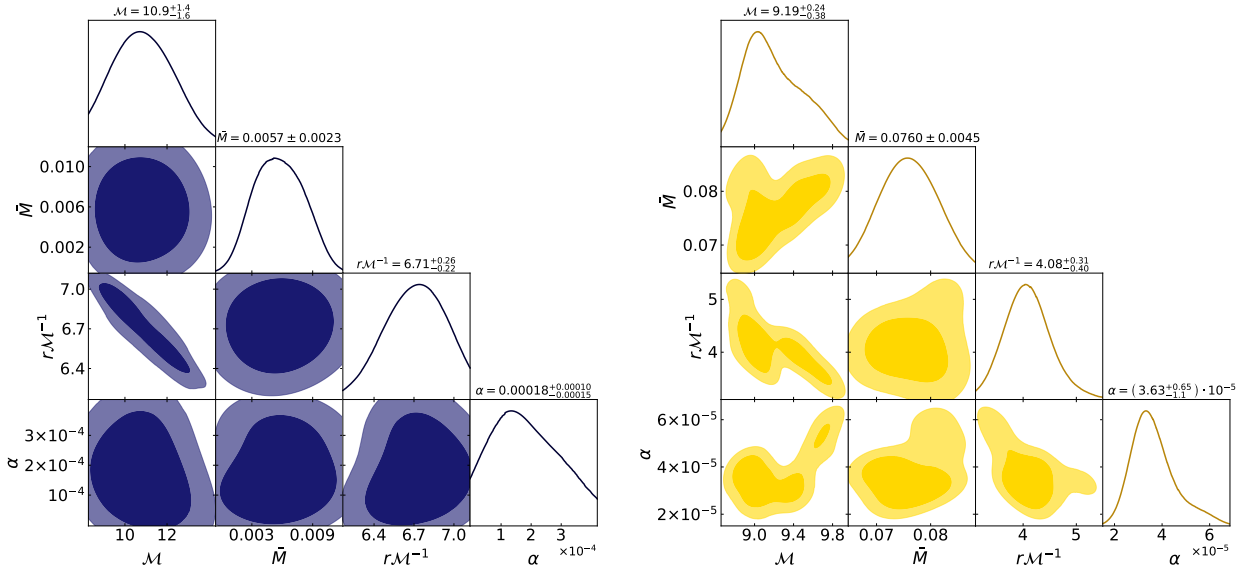


FIG. 8. MCMC outputs, showing the constraints on the parameters \mathcal{M} , \bar{M} , $r\mathcal{M}^{-1}$ and α , using data from GRS 1915+105 (left) and 1743–322 (right) BHs.

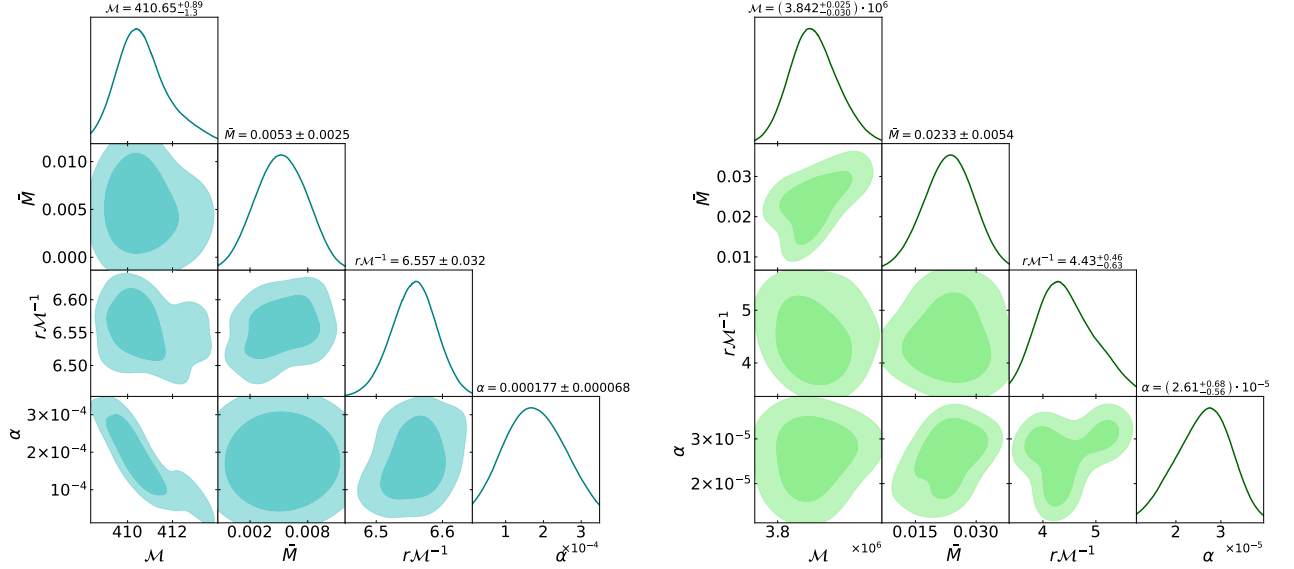


FIG. 9. MCMC outputs, showing the constraints on the parameters \mathcal{M} , \bar{M} , $r\mathcal{M}^{-1}$ and α , using data from M82 X-1 (left) and Sgr A* (right) BHs.

where v_{ob} and v_{th} are the observed and theoretical values of QPO frequencies. In Table III, the 3rd column presents the deviations of the theoretical upper QPO frequencies from the observed values, while the 5th column shows the deviations of the theoretical lower QPO frequencies from the observed values. From this table, it is evident that the deviation between the observed and theoretical QPO frequencies is higher for stellar-mass and intermediate-mass BHs, whereas for the supermassive BH Sgr A* the deviation is comparatively small.

VII. SUMMARY AND CONCLUSION

The main goal of this work is to study the circular motion of a test particle around the BHs in the presence of a gravitational trace anomaly, viz., the GB trace anomaly and then to study the effect of this trace anomaly on the QPOs of BHs using different theoretical models. The findings of the study are summarised as follows.

TABLE II. Estimated values of the parameters \mathcal{M} , \bar{M} , $r.\mathcal{M}^{-1}$, and α derived from the MCMC analysis.

BH	\mathcal{M}	\bar{M}	$r.\mathcal{M}^{-1}$	α
GRO J1655–40	6.03 ± 0.34	0.0036 ± 0.0018	$4.88^{+0.32}_{-0.40}$	$(3.49^{+0.95}_{-1.1}) \times 10^{-5}$
XTE J1550–564	9.29 ± 0.86	0.0048 ± 0.0023	6.15 ± 0.13	$(1.31 \pm 0.42) \times 10^{-4}$
GRS 1915+105	$10.9^{+1.4}_{-1.6}$	0.0057 ± 0.0023	$6.71^{+0.26}_{-0.22}$	$(1.80^{+0.10}_{-0.15}) \times 10^{-4}$
H 1743+322	$9.19^{+0.24}_{-0.38}$	0.0760 ± 0.0045	$4.08^{+0.31}_{-0.40}$	$(3.63^{+0.65}_{-1.1}) \times 10^{-5}$
M82 X-1	$410.65^{+0.89}_{-1.3}$	0.0053 ± 0.0025	6.557 ± 0.032	$(1.77 \pm 0.68) \times 10^{-4}$
Sgr A*	$(3.842^{+0.025}_{-0.030}) \times 10^6$	0.0233 ± 0.0054	$4.43^{+0.46}_{-0.63}$	$(2.61^{+0.68}_{-0.56}) \times 10^{-5}$

TABLE III. Theoretical QPO frequencies as obtained from the RP model and their deviations from the corresponding observed values of chosen BH sources.

BH	Upper Frequency (Hz)	Δv_U (%)	Lower Frequency (Hz)	Δv_L (%)
GRO J1655–40	497.87	12.69	317.26	6.4
XTE J1550–564	221.96	10.13	157.95	14.15
GRS 1915+105	198.71	18.27	127.97	12.91
H 1743+322	209.29	13.5	134.35	19.06
M82 X-1	5.57	11.24	3.96	19.27
Sgr A*	1.33×10^{-3}	7.63	0.81×10^{-3}	8.57

In the first subsection of Section III, we examined the equations of motion for a test particle orbiting a BH under the influence of the GB trace anomaly. Fig. 1 presents the variation of the effective potential with the GB trace anomaly parameter α , showing that the peak of the potential increases as α grows. In the second subsection, we investigated the properties of circular orbits. Fig. 2 depicts the dependence of the angular momentum \mathcal{J} and the specific energy \mathcal{E} on $r.\mathcal{M}^{-1}$ in the left and middle panels, respectively, while the right panel illustrates the variation of \mathcal{E} with \mathcal{J} . It is evident from Fig. 2 that the GB trace anomaly influence the motion of particle compared to the GR case. In the third subsection, we analyzed the behavior of the innermost stable circular orbit as a function of α for different values of \bar{M} as shown in Fig. 3.

In Section IV we studied the fundamental frequencies, i.e., Keplerian frequency and harmonic oscillation frequencies. In Subsection A, we calculated the Keplerian frequency Ω_ϕ and studied the variation of $\Omega_\phi.\mathcal{M}^{-1}$ with respect to $r.\mathcal{M}^{-1}$. It is found that Keplerian frequency decreases with the radial distance and increases with the magnitude of the GB trace anomaly factor α . The radial and vertical oscillation frequencies were calculated in Subsection B.

In Subsection A of Section V we discussed the different QPO models, viz., PR, RP, WD, TD and ER2–ER4 models. In this subsection, Fig. 5 shows the relation between upper QPO frequency ν_U and lower QPO frequency ν_L calculated using those models, for different values of α . This figure also includes reference lines for characteristic frequency ratios, with shaded regions between them marking distinct frequency ratio bands of twin-peak QPOs. It can be concluded from Fig. 5 that with higher values of α the relation between ν_U and ν_L deviates from the Schwarzschild case, highlighting the significant influence of the GB trace anomaly on QPO behaviour. In Subsection B, we have shown the dependence of QPO orbital radius with respect to α for frequency ratios 1:1, 3:2, 4:3 and 5:4 for all the above mentioned models along with the ISCO. It is clear from Fig. 6 that for the ER3 and TD models, the QPOs arise from significantly higher orbital radius. The ER2 and PR models also predict larger resonance radii. Moreover, the smallest QPO orbital is predicted by the RP model. It is to be noted that in all the models $r.\mathcal{M}^{-1}$ increases with α .

In Section VI, we constrained the parameters of the considered BHs using an MCMC analysis. For this purpose, we employed mass and QPO data from six different BH systems, as listed in Table I. The parameter priors were assumed to follow Gaussian distributions, as defined in Eq. (38). The log-likelihood functions for the upper and lower QPO frequencies are given in Eqs. (40) and (41), respectively. The results obtained from the MCMC analysis are summarized in Table II. As evident from the table, the constrained parameters also satisfy the condition in Eq. (16), which is a necessary requirement for the GB trace anomaly induced BHs. Furthermore, we calculated the theoretical values of the upper and lower QPO frequencies of the considered BHs for the RP QPO model using the parameter values obtained from the constraints. Our results show that the deviation between the observed and theoretical QPO frequencies is larger for the stellar-mass and intermediate-mass BHs, while for the supermassive BH Sgr A*, the deviation is comparatively small.

In conclusion, our analysis demonstrates that the GB trace anomaly has a significant effect on both the geodesic motion of test particles and the QPO properties of BHs predicted by various theoretical models. The anomaly not only varies the effective potential and the location of the ISCO but also significantly modifies the correlations between upper and lower QPO

frequencies, as well as the resonance radii in different models. The MCMC analysis, incorporating observational data from different BH systems, provides parameter constraints consistent with the theoretical requirements for GB trace anomaly induced BHs, thereby supporting the viability of this framework in explaining observed QPO behaviour. This work can be extended by incorporating more higher-order corrections to the spacetime metric and can also be extended to rotating BH solutions within GB trace anomaly gravity.

ACKNOWLEDGEMENTS

UDG is thankful to the Inter-University Centre for Astronomy and Astrophysics (IUCAA), Pune, India for the Visiting Associateship of the institute.

Appendix: Expressions of \mathcal{J} , \mathcal{E} , Ω_r , Ω_θ and Ω_ϕ

$$\mathcal{J}^2 = \frac{r^2 \left\{ M^2 \left(38731r^6 - 24720r^5r_h - 10950r^4r_h^2 - 93960r^3r_h^3 - 24015r^2r_h^4 - 22368rr_h^5 + 65100r_h^6 \right) \alpha^2 + \bar{M}^2 \left[32400M^4r^6r_h^4 - 1800M^2r^3r_h^2(23r^3 - 24r^2r_h - 15rr_h^2 - 24r_h^3) \alpha + \left(-6979r^6 - 39120r^5r_h - 5850r^4r_h^2 - 19560r^3r_h^3 + 99435r^2r_h^4 + 53952rr_h^5 + 31500r_h^6 \right) \alpha^2 \right] \right\}}{M^2 \left(-116193r^6 + 49440r^5r_h + 18250r^4r_h^2 + 140940r^3r_h^3 + 33621r^2r_h^4 + 29824rr_h^5 - 83700r_h^6 \right) \alpha^2 + \bar{M}^2 \left[32400M^4r^6(2r - 3r_h)r_h^3 + 1800M^2r^3r_h^2(69r^3 - 48r^2r_h - 25rr_h^2 - 36r_h^3) \alpha + \left(20937r^6 + 78240r^5r_h + 9750r^4r_h^2 + 29340r^3r_h^3 - 139209r^2r_h^4 - 71936rr_h^5 - 40500r_h^6 \right) \alpha^2 \right]} \quad (\text{A.1})$$

$$\mathcal{E}^2 = \left(1 - \frac{r_h}{r} \right) \left(1 + \frac{(23r^2 + 11rr_h + 6r_h^2)\alpha}{18M^2r^3r_h} - \frac{e^{-2\phi}M^2(38731r^5 + 26371r^4r_h + 22721r^3r_h^2 - 769r^2r_h^3 - 5572rr_h^4 - 9300r_h^5)\alpha^2}{32400\bar{M}^2M^4r^6r_h^3} - \frac{\bar{M}^2(6979r^5 + 26539r^4r_h + 28489r^3r_h^2 + 33379r^2r_h^3 + 13492rr_h^4 + 4500r_h^5)\alpha^2}{32400\bar{M}^2M^4r^6r_h^3} \right) \times \left(\frac{M^2(38731r^6 - 24720r^5r_h - 10950r^4r_h^2 - 93960r^3r_h^3 - 24015r^2r_h^4 - 22368rr_h^5 + 65100r_h^6)\alpha^2 + e^{2\phi}\bar{M}^2[32400M^4r^6r_h^4 - 1800M^2r^3r_h^2(23r^3 - 24r^2r_h - 15rr_h^2 - 24r_h^3)\alpha + (-6979r^6 - 39120r^5r_h - 5850r^4r_h^2 - 19560r^3r_h^3 + 99435r^2r_h^4 + 53952rr_h^5 + 31500r_h^6)\alpha^2]}{M^2(-116193r^6 + 49440r^5r_h + 18250r^4r_h^2 + 140940r^3r_h^3 + 33621r^2r_h^4 + 29824rr_h^5 - 83700r_h^6)\alpha^2 + e^{2\phi}\bar{M}^2[32400M^4r^6(2r - 3r_h)r_h^3 + 1800M^2r^3r_h^2(69r^3 - 48r^2r_h - 25rr_h^2 - 36r_h^3)\alpha + (20937r^6 + 78240r^5r_h + 9750r^4r_h^2 + 29340r^3r_h^3 - 139209r^2r_h^4 - 71936rr_h^5 - 40500r_h^6)\alpha^2]} \right) \quad (\text{A.2})$$

$$\Omega_r = \sqrt{\frac{(2\mathcal{M} - r)}{518400\mathcal{M}^3M^4r^8\bar{M}^2} \left(\begin{aligned} &144000\alpha^2\mathcal{M}^5\bar{M}^2 + 172800\alpha\mathcal{M}^4M^2r^3\bar{M}^2 + 215872\alpha^2\mathcal{M}^4r\bar{M}^2 + 259200\mathcal{M}^3M^4r^6\bar{M}^2 \\ &+ 158400\alpha\mathcal{M}^3M^2r^4\bar{M}^2 + 267032\alpha^2\mathcal{M}^3r^2\bar{M}^2 + 165600\alpha\mathcal{M}^2M^2r^5\bar{M}^2 + 113956\alpha^2\mathcal{M}^2r^3\bar{M}^2 \\ &+ 53078\alpha^2\mathcal{M}r^4\bar{M}^2 + 6979\alpha^2r^5\bar{M}^2 + 297600\alpha^2\mathcal{M}^5M^2 + 89152\alpha^2\mathcal{M}^4M^2r \\ &+ 6152\alpha^2\mathcal{M}^3M^2r^2 - 90884\alpha^2\mathcal{M}^2M^2r^3 - 52742\alpha^2\mathcal{M}M^2r^4 - 38731\alpha^2M^2r^5 \end{aligned} \right)} \quad (\text{A.3})$$

$$\Omega_\theta = \Omega_\phi = \frac{1}{720} \sqrt{\frac{2016000 \alpha^2 \mathcal{M}^6 \bar{M}^2 + 1382400 \alpha \mathcal{M}^5 M^2 r^3 \bar{M}^2 + 1726464 \alpha^2 \mathcal{M}^5 r \bar{M}^2 + 518400 \mathcal{M}^4 M^4 r^6 \bar{M}^2 + 432000 \alpha \mathcal{M}^4 M^2 r^4 \bar{M}^2 + 1590960 \alpha^2 \mathcal{M}^4 r^2 \bar{M}^2 + 345600 \alpha \mathcal{M}^3 M^2 r^5 \bar{M}^2 - 156480 \alpha^2 \mathcal{M}^3 r^3 \bar{M}^2 - 165600 \alpha \mathcal{M}^2 M^2 r^6 \bar{M}^2 - 23400 \alpha^2 \mathcal{M}^2 r^4 \bar{M}^2 - 78240 \alpha^2 \mathcal{M} r^5 \bar{M}^2 - 6979 \alpha^2 r^6 \bar{M}^2 + 4166400 \alpha^2 \mathcal{M}^6 M^2 - 715776 \alpha^2 \mathcal{M}^5 M^2 r - 384240 \alpha^2 \mathcal{M}^4 M^2 r^2 - 751680 \alpha^2 \mathcal{M}^3 M^2 r^3 - 43800 \alpha^2 \mathcal{M}^2 M^2 r^4 - 49440 \alpha^2 \mathcal{M} M^2 r^5 + 38731 \alpha^2 M^2 r^6}{\mathcal{M}^3 M^4 r^9 \bar{M}^2}} \quad (\text{A.4})$$

- [1] B. P. Abbott et al., *Observation of Gravitational Waves from a Binary Black Hole Merger*, *Phys. Rev. Lett.* **116**, 061102 (2016).
- [2] B. P. Abbott et al., *GW151226: Observation of Gravitational Waves from a 22-Solar-Mass Binary Black Hole Coalescence*, *Phys. Rev. Lett.* **116**, 241103 (2016).
- [3] B. P. Abbott et al., *GW170817: Observation of Gravitational Waves from a Binary Neutron Star Inspiral*, *Phys. Rev. Lett.* **119**, 161101 (2017).
- [4] R. Abbott et al., *GW190412: Observation of a Binary-Black-Hole Coalescence with Asymmetric Masses*, *Phys. Rev. D* **102**, 043015 (2020).
- [5] R. Abbott et al., *Observation of Gravitational Waves from Two Neutron Star–Black Hole Coalescences*, *Astrophys. J. Lett.* **915**, L5 (2021).
- [6] The Event Horizon Telescope Collaboration, *First M87 Event Horizon Telescope Results. IV. Imaging the Central Supermassive Black Hole*, *Astrophys. J. Lett.* **875**, L4 (2019).
- [7] The Event Horizon Telescope Collaboration, *First M87 Event Horizon Telescope Results. II. Array and Instrumentation*, *Astrophys. J. Lett.* **875**, L2 (2019).
- [8] The Event Horizon Telescope Collaboration, *First M87 Event Horizon Telescope Results. III. Data Processing and Calibration*, *Astrophys. J. Lett.* **875**, L3 (2019).
- [9] The Event Horizon Telescope Collaboration, *First M87 Event Horizon Telescope Results and the Role of ALMA*, *The Messenger* **177**, 25 (2019).
- [10] The Event Horizon Telescope Collaboration, *First M87 Event Horizon Telescope Results. V. Physical Origin of the Asymmetric Ring*, *Astrophys. J. Lett.* **875**, L5 (2019).
- [11] The Event Horizon Telescope Collaboration, *First M87 Event Horizon Telescope Results. VI. The Shadow and Mass of the Central Black Hole*, *Astrophys. J. Lett.* **875**, L6 (2019).
- [12] A. G. Riess et al., *Observational evidence from supernovae for an accelerating universe and a cosmological constant*, *Astron. J.* **116**, 1009 (1998).
- [13] F.-Q. Tu et al., *Accelerated expansion of the universe based on emergence of space and thermodynamics of the horizon*, *Phys. Lett. B* **784**, 411 (2018).
- [14] C. Pérez de los Heros, *Status, Challenges and Directions in Indirect Dark Matter Searches*, *Symmetry* **12**, 1648 (2020).
- [15] N. A. Bahcall et al., *The Cosmic Triangle: Assessing the State of the Universe*, *Science* **284**, 1481 (1999).
- [16] M. K. Gaillard, P. D. Grannis, and F. J. Sciulli, *The Standard model of particle physics*, *Rev. Mod. Phys.* **71**, S96 (1999), arXiv:hep-ph/9812285.
- [17] T. W. B. Kibble, *The Standard Model of Particle Physics*, arXiv:1412.4094 [physics.hist-ph] (2014).
- [18] W. A. Horowitz, *An extremely brief introduction to quantum field theory*, *J. Phys. Conf. Ser.* **802**, 012003 (2017).
- [19] F. Wilczek, *Quantum field theory*, *Rev. Mod. Phys.* **71**, S85 (1999), arXiv:hep-th/9803075.
- [20] A. Ashtekar and E. Bianchi, *A short review of loop quantum gravity*, *Rept. Prog. Phys.* **84**, 042001 (2021).
- [21] C. Rovelli, *Loop quantum gravity*, *Living Rev. Rel.* **1**, 1 (1998).
- [22] H. Sahlmann, *Loop Quantum Gravity - A Short Review*, arXiv:1001.4188 [gr-qc].
- [23] F. Girelli, F. Hinterleitner, and S. Major, *Loop Quantum Gravity Phenomenology: Linking Loops to Observational Physics*, *SIGMA* **8**, 098 (2012).
- [24] J. L. F. Barbon, *String theory*, *Eur. Phys. J. C* **33**, S67 (2004).
- [25] E. T. Akhmedov, *Review of modern string theory*, *Phys. Atom. Nucl.* **72**, 1574 (2009).
- [26] S. B. Giddings, *Is string theory a theory of quantum gravity?*, *Found. Phys.* **43**, 115 (2013).
- [27] J. Maharana, *Quantum gravity and string theory*, *18th Conference of the Indian Association for General Relativity and Gravitation*, 155 (1996).
- [28] J. Bedford, *An Introduction to String Theory*, arXiv:1107.3967 [hep-th].
- [29] A. Ashtekar, *New Hamiltonian formulation of general relativity*, *Phys. Rev. D* **36**, 1587 (1987).
- [30] C. Rovelli, *Ashtekar formulation of general relativity and loop space nonperturbative quantum gravity: A Report*, *Class. Quant. Grav.* **8**, 1613 (1991).

- [31] J. F. Donoghue, *General relativity as an effective field theory: The leading quantum corrections*, *Phys. Rev. D* **50**, 3874 (1994).
- [32] J. F. Donoghue, *Introduction to the effective field theory description of gravity*, [arXiv:gr-qc/9512024](#).
- [33] S. Faller, *Effective field theory of gravity: Leading quantum gravitational corrections to Newton's and Coulomb's law*, *Phys. Rev. D* **77**, 124039 (2008).
- [34] L. I. Bevilaqua, A. C. Lehum, and A. J. da Silva, *Effective field theory of quantum gravity coupled to scalar electrodynamics*, *Class. Quant. Grav.* **33**, 095008 (2016).
- [35] D. Wallace, *Quantum Gravity at Low Energies*, [arXiv:2112.12235 \[gr-qc\]](#).
- [36] R. J. Borah and U. D. Goswami, *Quasinormal modes and shadows of black holes in infinite derivative theory of gravity*, [arXiv:2504.20725 \[gr-qc\]](#) (2025).
- [37] J. F. Donoghue and B. R. Holstein, *Low Energy Theorems of Quantum Gravity from Effective Field Theory*, *J. Phys. G* **42**, 103102 (2015).
- [38] Konoplya, R. A. and Zhidenko, A., Quasinormal modes of black holes: From astrophysics to string theory, *Rev. Mod. Phys.* **83**, 793 (2011).
- [39] Berti, E., Black hole quasinormal modes: Hints of quantum gravity?, *Conf. Proc. C* 0405132, 145 (2004).
- [40] J. H. Traschen, *An introduction to black hole evaporation*, in *Proceedings of the 1999 Londrina Winter School on Mathematical Methods in Physics*, [arXiv:gr-qc/0010055](#) (1999).
- [41] M. F. Wondrak, W. D. van Suijlekom, and H. Falcke, *Gravitational pair production and black hole evaporation*, *Phys. Rev. Lett.* **130**, 221502 (2023).
- [42] F. Holdt-Sørensen, D. A. McGady, and N. Wintergerst, *Black hole evaporation and semiclassicality at large D*, *Phys. Rev. D* **102**, 026016 (2020).
- [43] V. Husain and S. Singh, *Quantum backreaction on a classical universe*, *Phys. Rev. D* **104**, 124048 (2021), [arXiv:2109.12752 \[gr-qc\]](#).
- [44] M. Casals, A. Fabbri, C. Martínez, and J. Zanelli, *Quantum backreaction on three-dimensional black holes and naked singularities*, *Phys. Rev. Lett.* **118**, 131102 (2017), [arXiv:1608.05366 \[gr-qc\]](#).
- [45] R. H. Brandenberger, *Introduction to early universe cosmology*, *PoS ICFI2010*, 001 (2010), [arXiv:1103.2271 \[astro-ph.CO\]](#).
- [46] A. Mondal and R. N. Raveendran, *Early universe cosmology with coherent state as an initial choice*, [arXiv:2410.04608 \[gr-qc\]](#) (2024).
- [47] U. D. Goswami, *Supersymmetric hybrid inflation with non-minimal coupling to gravity*, *Eur. Phys. J. Plus* **135**, 44 (2020), [arXiv:1705.05540 \[astro-ph.CO\]](#).
- [48] S. Hollands, Á. D. Kovács, and H. S. Reall, *The second law of black hole mechanics in effective field theory*, *JHEP* **08**, 258 (2022), [arXiv:2205.15341 \[hep-th\]](#).
- [49] I. Davies and H. S. Reall, *Nonperturbative second law of black hole mechanics in effective field theory*, *Phys. Rev. Lett.* **132**, 171402 (2024).
- [50] D. J. Gogoi and U. D. Goswami, *Quasinormal modes and Hawking radiation sparsity of GUP corrected black holes in bumblebee gravity with topological defects*, *JCAP* **06** (2022) 029, [arXiv:2203.07594 \[gr-qc\]](#).
- [51] R. Karmakar, D. J. Gogoi and U. D. Goswami, *Quasinormal modes and thermodynamic properties of GUP-corrected Schwarzschild black hole surrounded by quintessence*, *Int. J. Mod. Phys. A* **37**, 2250180 (2022), [arXiv:2206.09081 \[gr-qc\]](#).
- [52] S. Mukohyama *et al.*, *Quasinormal modes from EFT of black hole perturbations with timelike scalar profile*, *JCAP* **07**, 050 (2023), [arXiv:2304.14304 \[gr-qc\]](#).
- [53] W. Liu, D. Wu and J. Wang, *Light rings and shadows of static black holes in effective quantum gravity*, *Phys. Lett. B* **858**, 139052 (2024), [ScienceDirect](#).
- [54] Z. L. Wang and E. Battista, *Dynamical features and shadows of quantum Schwarzschild black hole in effective field theories of gravity*, *Eur. Phys. J. C* **85**, 304 (2025), [arXiv:2501.14516 \[gr-qc\]](#).
- [55] R. Karmakar and U. D. Goswami, *Quasinormal modes, thermodynamics and shadow of black holes in Hu–Sawicki $f(R)$ gravity theory*, *Eur. Phys. J. C* **84**, 969 (2024), [arXiv:2406.18329 \[gr-qc\]](#).
- [56] L. S. Brown and J. P. Cassidy, *Stress-tensor trace anomaly in a gravitational metric: General theory, Maxwell field*, *Phys. Rev. D* **15**, 2810 (1977).
- [57] E. Mottola, *New Horizons in Gravity: The Trace Anomaly, Dark Energy and Condensate Stars*, *Acta Phys. Polon. B* **41**, 2031 (2010).
- [58] M. Calzá, A. Casalino and L. Sebastiani, *Local solutions of general relativity in the presence of the trace anomaly*, *Phys. Dark Univ.* **37**, 101066 (2022).
- [59] A. Ingram and S. Motta, *A review of quasi-periodic oscillations from black hole X-ray binaries: observation and theory*, *New Astron. Rev.* **85**, 101524 (2019), [arXiv:2001.08758 \[astro-ph.HE\]](#).
- [60] A. Davlataliev *et al.*, *Quasi periodic oscillations around Kerr-type black hole in the Starobinsky–Bel–Robinson theory of gravity*, *Phys. Dark Univ.* **46**, 101569 (2024).
- [61] S. E. Motta, *Quasi periodic oscillations in black hole binaries*, *Astron. Nachr.* **337**, 398 (2017), [arXiv:1603.07885 \[astro-ph.HE\]](#).
- [62] T. M. Belloni, A. Sanna and M. Méndez, *High-frequency quasi-periodic oscillations in black hole binaries*, *Mon. Not. Roy. Astron. Soc.* **426**, 1701 (2012).
- [63] P. Rana and A. Mangalam, *A geometric origin for quasi-periodic oscillations in black hole X-ray binaries*, *Astrophys. J.* **903**, no.2, 121 (2020), [arXiv:2009.01832 \[astro-ph.HE\]](#).
- [64] B. Hazarika, M. M. Gohain and P. Phukon, *Signatures of NED on quasi periodic oscillations of a magnetically charged black hole*, *JCAP* **07**, 035 (2025).
- [65] B. Hazarika and P. Phukon, *Probing Black Hole Phase Transitions through Quasi-Periodic Oscillations*, [arXiv:2504.11205 \[gr-qc\]](#) (2025).
- [66] D. Altamirano and T. Strohmayer, *Low-frequency (11 mHz) oscillations in H1743-322: A new class of black hole quasi-periodic oscillations?*, *Astrophys. J.* **754**, L23 (2012).

- [67] M. Mandal and S. Pal, *Detection of low-frequency QPO from X-ray pulsar XTE J1858+034 during outburst in 2019 with NuSTAR*, [arXiv:2101.09250 \[astro-ph.HE\]](#).
- [68] Z. Yan, S. Rapisarda and W. Yu, *Detection of a low-frequency quasi-periodic oscillation in the soft state of Cygnus X-1 with Insight-HXMT*, *Astrophys. J.* **919**, 46 (2021).
- [69] T. M. Belloni, A. Sanna and M. Méndez, *High-frequency quasi-periodic oscillations in black hole binaries: HFQPO in black hole binaries*, *Mon. Not. R. Astron. Soc.* **426**, 1701 (2012).
- [70] P. C. Fragile, O. Straub and O. Blaes, *High-Frequency and Type-C QPOs from Oscillating, Precessing Hot, Thick Flow*, *Mon. Not. R. Astron. Soc.* **461**, 1356 (2016).
- [71] L. Angelini, L. Stella and A. N. Parmar, *The Discovery of 0.2 Hz Quasi-periodic Oscillations in the X-Ray Flux of the Transient 42 Second Pulsar EXO 2030+374*, *Astrophys. J.* **346**, 906 (1989).
- [72] H. Zhang, L. Meng, L. Zhang and B. Dai, *Revisiting the observation–theory confrontation in high-frequency QPOs: a new QPO in NGC 5506, intermediate-mass black holes, and the crucial role of accretion state*, *Mon. Not. R. Astron. Soc.* **538**, 2161 (2025).
- [73] F. Abdulkhamidov *et al.*, *Explaining QPOs data for black holes in the Starobinsky–Bel–Robinson gravity*, *Eur. Phys. J. C* **84**, 420 (2024).
- [74] G. Mustafa *et al.*, *Testing Quantum-Corrected Black Holes with QPOs Observations: A Study of Particle Dynamics and Accretion Flow*, [arXiv:2506.16405 \[gr-qc\]](#) (2025).
- [75] S. Tsujikawa, *Black holes in a new gravitational theory with trace anomalies*, *Phys. Lett. B* **843**, 138054 (2023).
- [76] G. Gabadadze, *A new gravitational action for the trace anomaly*, *Phys. Lett. B* **843**, 138031 (2023).
- [77] D. Friedan, Z. Qiu and S. Shenker, *Conformal Invariance, Unitarity, and Critical Exponents in Two Dimensions*, *Phys. Rev. Lett.* **52**, 1575 (1984).
- [78] Z. Komargodski and A. Schwimmer, *On Renormalization Group Flows in Four Dimensions*, *JHEP* **12**, 099 (2011).
- [79] J. L. Cardy, *Is there a c-theorem in four dimensions?*, *Phys. Lett. B* **215**, 749 (1988).
- [80] J. Shokhzod *et al.*, *Circular motion and QPOs near black holes in Kalb–Ramond gravity*, *Eur. Phys. J. C* **84**, 964 (2024).
- [81] S. Jumaniyozov *et al.*, *Collisions and dynamics of particles with magnetic dipole moment and electric charge near magnetized rotating Kerr black holes*, *Eur. Phys. J. C* **84**, 291 (2024).
- [82] T. Xamidov *et al.*, *Quasiperiodic oscillations around a Schwarzschild black hole surrounded by a Dehnen type dark matter halo*, *Phys. Dark Univ.* **47**, 101805 (2025).
- [83] M. Shahzadi, M. Kološ, Z. Stuchlík, and Y. Habib, *Epicyclic oscillations in spinning particle motion around Kerr black hole applied in models fitting the quasi-periodic oscillations observed in microquasars and AGNs*, *Eur. Phys. J. C* **81**, 1067 (2021).
- [84] W. Kluźniak and M. A. Abramowicz, *Parametric epicyclic resonance in black hole disks: QPOs in micro-quasars*, [arXiv:astro-ph/0203314](#).
- [85] M. A. Abramowicz, V. Karas, W. Kluźniak, W. H. Lee, and P. Rebusco, *Nonlinear resonance in nearly geodesic motion in low mass X-ray binaries*, *Publ. Astron. Soc. Jpn.* **55**, 467 (2003).
- [86] L. Stella and M. Vietri, *Lense-Thirring precession and QPOs in low mass X-ray binaries*, *Astrophys. J. Lett.* **492**, L59 (1998).
- [87] L. Stella and M. Vietri, *kHz quasi-periodic oscillations in low mass X-ray binaries as probes of general relativity in the strong field regime*, *Phys. Rev. Lett.* **82**, 17 (1999).
- [88] S. M. Morsink and L. Stella, *Relativistic precession around rotating neutron stars: effects due to frame-dragging and stellar oblateness*, *Astrophys. J.* **513**, 827 (1999).
- [89] S. Kato, *Wave-warp resonant interactions in relativistic disks and kHz QPOs*, *Publ. Astron. Soc. Jpn.* **56**, 559 (2004).
- [90] S. Kato, *Excitation of disk oscillations by warps: A model of kHz QPOs*, *Publ. Astron. Soc. Jpn.* **56**, 905 (2004).
- [91] U. Kostić, A. Čadež, M. Calvani, and A. Gomboc, *Tidal effects on small bodies by massive black holes*, *Astron. Astrophys.* **496**, 307 (2009).
- [92] M. E. Beer and P. Podsiadlowski, *The quiescent light curve and evolutionary state of GRO J1655–40*, *Mon. Not. Roy. Astron. Soc.* **331**, 351 (2002).
- [93] S. E. Motta, T. M. Belloni, L. Stella, T. Muñoz-Darias, and R. Fender, *Precise mass and spin measurements for a stellar-mass black hole through X-ray timing: the case of GRO J1655–40*, *Mon. Not. Roy. Astron. Soc.* **437**, 2554 (2014).
- [94] J. A. Orosz *et al.*, *An improved dynamical model for the microquasar XTE J1550–564*, *Astrophys. J.* **730**, 75 (2011).
- [95] M. J. Reid *et al.*, *A parallax distance to the microquasar GRS 1915+105 and a revised estimate of its black hole mass*, *Astrophys. J.* **796**, 2 (2014).
- [96] G. Pei *et al.*, *Blandford–Znajek mechanism in black holes in alternative theories of gravity*, *Eur. Phys. J. C* **76**, 534 (2016).
- [97] A. Bhattacharjee *et al.*, *The 2004 outburst of BHC H1743–322: Analysis of spectral and timing properties using the TCAF solution*, *Mon. Not. Roy. Astron. Soc.* **466**, 1372 (2017).
- [98] J. Petri, *A new model for QPOs in accreting black holes: application to the microquasar GRS 1915+105*, *Astrophys. Space Sci.* **318**, 181 (2008).
- [99] D. R. Pasham *et al.*, *A 400-solar-mass black hole in the galaxy M82*, *Nature* **513**, 74 (2014).
- [100] A. M. Ghez *et al.*, *Measuring distance and properties of the Milky Way’s central supermassive black hole with stellar orbits*, *Astrophys. J.* **689**, 1044 (2008).
- [101] S. Gillessen *et al.*, *Monitoring stellar orbits around the massive black hole in the Galactic Center*, *Astrophys. J.* **692**, 1075 (2009).
- [102] Z. Stuchlík and A. Kotrllová, *Orbital resonances in discs around braneworld Kerr black holes*, *Gen. Rel. Grav.* **41**, 1305 (2009).
- [103] C. Liu *et al.*, *Constraints on the rotating self-dual black hole with quasi-periodic oscillations*, *JCAP* **11**, 096 (2023), [arXiv:2305.12323 \[gr-qc\]](#).
- [104] S. Mitra *et al.*, *Charged particles and quasiperiodic oscillations in Black–bounce–Reissner–Nordström geometry in braneworlds*, *Phys. Dark Univ.* **46**, 101561 (2024).